COMPUTATIONAL FLUID DYNAMICS FOR MODELING AND SIMULATION OF INTRAOCULAR DRUG DELIVERY AND WALL SHEAR STRESS IN PULSATILE FLOW

A Thesis

Submitted to the Faculty

of

Purdue University

by

Seyedalireza Abootorabi

In Partial Fulfillment of the

Requirements for the Degree

of

Master of Science in Mechanical Engineering

August 2020

Purdue University

Indianapolis, Indiana

THE PURDUE UNIVERSITY GRADUATE SCHOOL
STATEMENT OF THESIS APPROVAL

Dr. Huidan Yu, Chair

Department of Mechanical and Energy Engineering

Dr. Hiroki Yokota

Department of Biomedical Engineering

Dr. Khosrow Nematollahi

Department of Mechanical and Energy Engineering

Approved by:

Dr. Sohel Anwar

Chair of the Graduate Program

To my parents and sister

ACKNOWLEDGMENTS

I cannot express enough thanks to my committee for their continued support and encouragement. Special thanks to my adviser and committee chair, Dr. Whitney Yu, who supported my research tirelessly. I want to thank my committee members Dr. Hiroki Yokota and Dr. Khosrow Nematollahi, who helped me relentlessly solve the scientific and writing issues of this dissertation. I offer my sincere appreciation for the learning opportunities provided by my committee members that continued until the very last moment of writing this thesis. My completion of this thesis could not have been accomplished without my lab-mates: Xiaoyu Zhang, Monsurul Islam Khan, Xin Jin, and Chenbin Rong. Special thanks to the people who helped me to modify this dissertation with their professional help: Dr. Nojan Aliahmad, Ehsan Malekipour, and Cheyenne Collins for helping me with this dissertation.

PREFACE

This research presents two different applications of computational fluid mechanics in the bio-engineering. In the first section of this thesis, the drug delivery in the posterior eye has been simulated using the finite element method. The simulation gives a valuable tool to the doctors who need to treat eye diseases with a specific range of drug dosage. The second section in the thesis studies the wall shear stress and velocity field in a rectangular duct. The accuracy of the measured shear stress is then compared in boundary cells. Having an accurate computational model is useful in bio-engineering and gives us better insight to understand the fluid-structure interaction in bodily organs.

TABLE OF CONTENTS

Page

LIST OF TABLES

LIST OF FIGURES

Figure Page

SYMBOLS

m	mass
v	velocity
P_v	P-value
p	pressure
Q	volumetric flow rate
t	time

ABBREVIATIONS

CFD	Computational Fluid Dynamics
BC	boundary condition
LBM	lattice Boltzmann method
LBE	lattice Boltzmann equation
LGA	lattice gas automata
VLBM	volumetric lattice Boltzmann method
FEM	finite element method
FVM	finite volume method
NS	Navier-Stokes
CPU	central processing unit
GPU	graphics processing unit
PDE	partial differential equation
AMD	age-related macular degeneration
FDA	food and drug administration
DNS	direct numerical simulation
LES	large eddy simulation
VEGF	vascular endothelial growth factor

ABSTRACT

Abootorabi, Seyedalireza, M.S.M.E, Purdue University, August 2020. Computational Fluid Dynamics for Modeling and Simulation of Intraocular Drug Delivery and Wall Shear Stress in Pulsatile Flow. Major Professor: Dr. Huidan Yu .

The thesis includes two application studies of computational fluid dynamics. The first is new and efficient drug delivery to the posterior part of the eye, a growing health necessity worldwide. Current treatment of eye diseases, such as age-related macular degeneration (AMD), relies on repeated intravitreal injections of drug-containing solutions. Such a drug delivery has significant drawbacks, including short drug life, vital medical service, and high medical costs. In this study, we explore a new approach of controlled drug delivery by introducing unique porous implants. Computational modeling contains physiological and anatomical traits. We simulate the IgG1 Fab drug delivery to the posterior eye to evaluate the effectiveness of the porous implants to control the drug delivery. The computational model was validated by established computation results from independent studies and experimental data. Overall, the results indicate that therapeutic drug levels in the posterior eye are sustained for eight weeks, similar to those performed with intravitreal injection of the same drug. We evaluate the effects of the porous implant on the time evaluation of the drug concentrations in the sclera, choroid, and retina layers of the eye. Subsequent simulations were carried out with varying porosity values of a porous episcleral implant. Our computational results reveal that the time evolution of drug concentration is distinctively correlated to drug source location and pore size. The response of this porous implant for controlled drug delivery applications was examined. A correlation between porosity and fluid properties for the porous implants was revealed in this study. The second application lays in the computational modeling of the oscillating

flow in rectangular ducts. This computational study has further applications in investigating the fluid flow motion in bodily organs. It can be useful in studying the response of bone cells to the wall shear stress in the human body.

1. INTRODUCTION

The prevalence of computational fluid dynamics (CFD) has caused a revolution in industrial and medical areas. Tackling problems in achieving high-performance computing (HPC), visualizing data, and providing an infrastructure for optimized methods of simulations have provided us with many advancements in other fields and were beneficial not only in the CFD realm. CFD is a powerful tool in harnessing information in medical fields where the experimental measures are either hard or impossible. In recent years, the Food and Drug Administration has put a lot of effort into fastening the approval process for the medical products. They have used the CFD in their research and development process. This has led to groundbreaking applications in various fields in engineering and medicine and has eased the legal process for medical system approvals. The CFD implementation has increased within the last years among experts in medical, environmental, agricultural, and many other industrial applications. It is crucial to have the fundamental knowledge of fluid mechanics to make an appropriate initial assumption to simulate the phenomena correctly or, if possible, make a user-friendly interface. For example, if we narrow down our attention to medical science and use CFD tools in clinical decisions, we need to tune the output for each specific case. Although the CFD application is growing every day, major challenges exist, such as computational speed, mathematical modeling defects, computer power limits, etc. In this dissertation, we are going to study two applications of Computational Fluid Dynamics (CFD) in Biomedical Engineering. In the first application, we are going to study drug delivery in the posterior eye. This study involves the computational solving of the non-linear Navier-Stokes equations and the mass diffusion equation. At the second application, we will use the volumetric lattice Boltzmann method (VLBM) to compute wall-shear stress and velocity distribution inside a rectangular duct.

1.1 Computational Fluid Dynamics (CFD)

The fundamental equations that describe the motion of the flow are Navier-Stokes (NS) equations. Due to the highly non-linear structure of these equations, it is difficult to find an analytical solution. To this day, an analytical solution for NS equations remains an open problem to solve. Another way to solve the NS equations is with numerical methods. However, the numerical solution of these equations requires a large number of iterations and is massively time-consuming. The conventional approach to solve NS equations is the Direct Numerical Solution (DNS). This method is generally considered the most straightforward method in Computational Fluid Dynamics. However, this method requires a large memory and is slow compared to other methods, such as the Lattice-Boltzmann Method (LBM). The computational cost for this method is high, even at low Reynolds numbers. In most industrial applications, DNS cannot be used even within the means of most powerful computers to this day. However, there are applications for this method at small Reynolds numbers, and there are many cases that we need to use DNS. The applicability of DNS is usually limited to low to moderate Reynolds numbers. There are other numerical methods for higher Reynolds numbers than can capture more details in simulation, such as Reynolds averaged Navier-Stokes (RANS) or Large Eddy Simulation (LES), which is excluded from the content of this thesis.

1.2 Objective

In this dissertation, we explore two different applications of computational fluid dynamics in Bio-engineering. At the first application, we present a new computational model by introducing a porous separator (or divider) within the drug storage (implant) and simulate the drug delivery to the posterior eye. The research objective is to avoid the overshooting of drug concentration at initial times and increase the average concentration at every time point. This can be done by changing the implant internal structure. The computational model focuses on the eye posterior layers

(sclera, choroid, and retina). We first validate our computational model by repeating the results in [1]. Then, we systematically investigate how the porous structure in the implant affects drug delivery. The second application aims to obtain an accurate computational model to simulate the pulsatile flow inside a rectangular duct. By getting a well-defining LBM model, we can proceed to use the computational code in simulating wall shear stress and velocity field inside similar domains, such as pulsatile flow over the bone cells. These results can be later used to research how the bone cells respond to the wall shear stress [2].

2. COMPUTATIONAL MODELING OF INTRAOCULAR DRUG DELIVERY SUPPLIED BY POROUS IMPLANTS

2.1 Introduction

Age-related macular degeneration (AMD) is a degenerative disease of the retina layer where uncontrolled growth of cells in the blood vessels causes protein and blood leakage and scars the macula (a part of the retina layer inside the eyeball). It is a condition that often results in blurred or no vision in the central visual field. Such vision loss is permanent, affecting people's ability to recognize faces, drive or perform daily activities. AMD is the leading cause of severe vision loss in people over age sixty years old (The National Eye Institute 2020). According to the National Eye Institute, as the elder population in the U.S. grows larger, more people are developing eye diseases. In fact, from 2000 to 2010 the number of elderly people with AMD grew 18 percent, from 1.75 million to 2.07 million (The National Eye Institute 2020). It is known that vascular endothelial growth factor (VEGF), a signal protein produced by cells that stimulate the formation of blood vessels, is responsible for this eye disease condition. Anti-VEGF drugs such as Ranibizumab, Macugen, and IgG1 Fab fragment are frequently used to treat AMD. An injection is a common way to deliver drugs for the treatment of AMD. However, this adds potential risks such as endophthalmitis, hemorrhage, and retinal detachment [3], among others. The oral consumption of drugs is an alternative but ineffective method to deliver the drug via blood flow. Since the blood supply into the human eye is small, a large amount of drug consumption is needed, which may put other non-diseased tissues in danger. Sclera permeability is a less risky, less invasive, and more sustainable drug transport method of drug delivery for AMD, enabling transscleral drug delivery [4]. In this type of drug delivery, an implant that contains a drug is implanted on the posterior eye (AMD normally affects

the posterior eye) and the drug diffuses into the eye slowly [5], providing a sustainable drug transport source. The two goals of using the drug implant is to reduce the high initial drug concentration in the eye, and to maintain a higher drug supply in later periods of the treatment.

It is essential to predict drug transport in the different layers of the posterior eye to design an effective delivery system. Drugs available for AMD have a narrow therapeutic concentration window (i.e. limited range of drug dosages which can treat the disease effectively without having toxic effects). Medication with such a restricted therapeutic window must, therefore, be administered with care and control. High drug concentrations can be harmful to the eye while low drug supply results in the ineffective treatment of AMD [6]. Therefore, it is crucially important to determine the time evolution of drug concentration in each layer in the posterior eye. There are experimental techniques available to measure drug concentration in the eye such as absorption spectroscopy [7] and direct sampling [8]. Some studies have emphasized the benefits and challenges of such experiments. Miller et al. (2005) [9] have reported minimally invasive and direct measurements of drug concentration in the eye via absorption spectroscopy whereas Conrad and Robinson (1977) [8] have described that direct sampling is possible but difficult for the patient.

Numerical simulation of drug delivery in the eye is a new and non-invasive method to measure the time evolution of drug concentration. This technique offers several advantages, including the ability to i) study a system or phenomenon at different length and time scales, ii) obtain reliable results, once well validated by available analytical and/or experimental data, iii) perform analysis of varied conditions, iv) evaluate critical situations that can be investigated without risk, and v) carry out cost-effective studies that can speed up so that system or phenomenon can be evaluated over a long time. Simulations are usually much faster than experiments. In the present study, we simulate 8-week drug delivery in less than 30 minutes with standard CPUs of personal computers. Some of the disadvantages of simulations of drug delivery in the eye include i) an understanding of the controlled drug delivery phenomena

is needed as well as the associated limitations and approximations of the model to discern the solutions from potential artifacts, and ii) limited experimental data [10] is available regarding posterior eye layers. Several simulation studies have been reported to date investigating the drug delivery in the eye computationally [11, 12], in which drug delivery from a standard implant in the posterior eye is simulated using the finite element method (FEM) and drug concentration evolution is calculated for different eye layers. Other studies [13–15] have focused on computational modeling to simulate the intravitreous drug injection in the human eye.

The thermally responsive hydrogel NIPAM has been used to evaluate ocular drug delivery computationally [11,16] by placing it on the sclera close to the optical nerve. Previous simulations of drug delivery from an episcleral (N-isopropyl acrylamide) NIPAM-gel implant by [16] predicted sustained delivery times of eight weeks with both 1.0 and 0.5 mg monthly doses using a compartmental model. Later, simulations by [11], using a computational model of IgG1 Fab delivery from an episcleral NIPAM-gel implant, released the drug at the same rate and monthly doses as in [16] in a new model of the human eye to determine the time needed for sustained delivery. Results from the latter study [11] show that the average drug concentration is at therapeutic levels within all three layers in the posterior eye during the first eight weeks after drug administration, similarly to those with intravitreal injection [15]. Kavaousanakis and co-workers (2014) [11] concluded that delivery of the IgG1 Fab drug from an episcleral NIPAM-gel implant seems to be an effective alternative to more invasive means of delivery to the posterior eye by injection. Thus, we used these results in our validation phase in this work. Since we need to keep the drug concentration in the desired therapeutic range, it is imperative to use the proper amount of drug concentration. It is noteworthy that we excluded the vitreous humor and confined our simulations to the eye posterior layers (sclera, choroid, and retina) from a porous implant.

In this study, we present a new computational model of a drug storage (implant) in which a porous separator (or divider) is introduced and simulate the drug delivery to the posterior eye. The research objective is to achieve an appropriate time evolution

of the drug concentration, avoiding the overshooting of drug concentration at initial times and increasing the later concentration. This can be done by changing the implant internal structure and including pores. We keep the drug concentration in the desired therapeutic range. The computational model includes the eye posterior layers (sclera, choroid, and retina) and drug storage. We first validate our computational model by repeating the results in [11]. Then, we systematically investigate how the porous structure in the implant affects drug delivery.

2.2 Computational Modeling and Governing Equations

To study the effects of implant structure on the drug delivery to the posterior eye, we created a model representative of the human eye together with an implant attached to the sclera layer on the back of the eye. Fig. 2.1.(a) illustrates a cross-sectional view of a human eye. The vitreous humor is a gel-like porous medium, which comprises most of the interior eye. It is enclosed by the retina layer on the posterior eye and by the lens and hyaloid membrane on the front side of the eye.

2.2.1 Human eye representative and computational modeling

The front side of the eye, i.e. lens and pupil, were not be taken into account in this study because they are almost impermeable to drugs as there is constant flow drainage between the iris and lens which washes any drug away. Since the transport of macromolecules such as IgG1 Fab is not significant in the front of the eye (cannot penetrate the hyaloid membrane) and the drug for the AMD targets the three posterior layers, the vitreous humor was not included in this study either. Fig. 2.1.(b) shows the 2D computational model consisting of posterior layers (retina, choroid, and sclera), and a drug storage implant with a porous structure. We used COMSOL Multiphysics version 5.4 (COMSOL, Inc., Burlington, MA) to simulate the delivery of IgG1 Fab drug from the porous implant to the posterior layers. The main physical property values and dimensions were based on experimental data [11, 12],

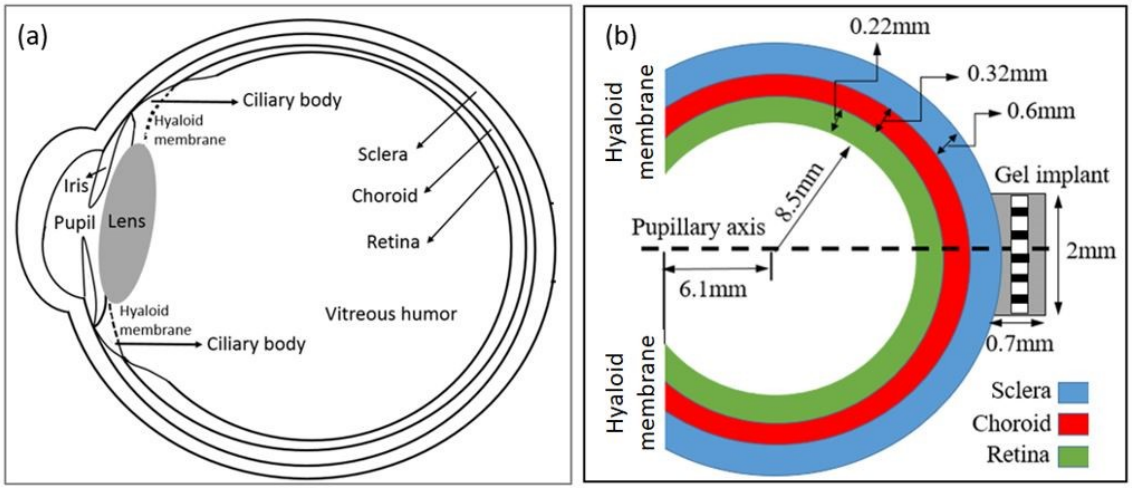

Fig. 2.1. Schematics of a cross-section of the human eye showing an episcleral implant and key features. (a) An anatomical view of the posterior segment consisting of three distinct layers (sclera, choroid, and retina). (b) Computational geometry involving the posterior layers (retina, choroid, and sclera) and a drug storage implant with a porous separator (white and black squares mean solid pieces and pores, respectively). Dimensions are to scale. Relevant dimensions and properties are listed in Table 2.1. Figure (b) shows a two-dimensional axisymmetric model of the eye and the axis of symmetry is shown as the dashed line in Figure (b). The domains shown in the figures are connected to each other and do not have separate boundary condition

as summarized in Table 2.1. Boundary conditions were introduced as follows. The pressure at the outer surface of the sclera layer, P_s (=1300 Pa) known as previously reported [17]. The pressure at the hyaloid membrane is equal to the intraocular pressure (retina layer), i.e. P_h (= 2000 Pa) [11].

The hyaloid membrane is a layer permeable to small drugs such as fluorescein but impermeable to heavier drug molecules such as IgG1 Fab. There is no concentration flux at the sclera and retina's external walls and the implant's walls, i.e., $\hat{n}\cdot\nabla c\,|_{wall}= 0$, in which n is the normal vector to the surface, D is the diffusion coefficient, and c is the drug concentration. The initial velocity is considered zero for the entire domain as well as zero concentration of the drug. The supply of the drug concentration in

the implant is given in Fig. 2.2.(b). The specific location of the drug supply will be identified later. The numbers of mesh in the radial direction are 3 in the retina and choroid layers and 4 in the sclera layer respectively. The number of mesh in the tangential direction is 1400. The distribution of the mesh in each direction is uniform. The convergence check is done for the considered mesh size.

The parameters used in the simulations for the transport of the IgG1 Fab fragment are summarized in Table 2.1.

There are several approximations in this study that must be pointed at:

- The concentration distribution is considered uniform all along the implant-sclera intersection
- The sclera, choroid and retina's properties are considered uniform in all part of them
- The hydrogel is considered to has a solid size and remain
- the experimental measurements are limited and more experiments are needed in order to enhance the simulation results
- The assumed geometry for the eye is not perfect sphere, but for the case of simplicity we have considered sphere in our simulation
- A three dimensional model would be more accurate in presenting the results but we are using a two dimensional axisymmetric model

2.2.2 Mathematical model and governing equations

The flow domain including sclera, choroid, and retina layers in Fig. 2.1.(b), is treated as a porous medium. The eye drug is stored in the implant and delivered to the posterior layers. As the flow in the sclera, choroid and retina layers is weak, we used the Darcy (creeping) flow equation. The creeping flow equation is coupled with

Table 2.1.
Physical property values for the posterior eye layers and implant in this study.

Parameter	Value	Source number
sclera (outer layer)	-	-
Hydraulic conductivity $(\mu/k)_s$	$1.5 \times 10^{-}11 cm^2/Pa.s$	[12, 18]
Thickness (d_s)	0.6 mm	[15]
Diffusivity (D_s)	$4.596 \times 10^{-}7 cm^2/s$	[16]
choroid (middle layer)	-	-
Hydraulic conductivity $(\mu/k)_c$	$1.5 \times 10^{-}11 cm^2/Pa.s$	[18]
Thickness (d_c)	0.32 mm	[15]
Diffiusivity (D_c)	3.616 x 10-8 cm2/s	[16]
Drug elimination rate constant (k_{ec})	0.2398 $day^{-}1$	[7]
retina (inner layer)	-	-
Hydraulic conductivity $(\mu/k)_r$	$2.36 \times 10^{-}11 cm^2/Pa.s$	[19]
Thickness (d_r)	0.22 mm	[15]
Diffuisivity (D_r)	$2.442 \times 10^{-}7 cm^2/s$	[16]
Drug elimination rate constant (k_{er})	0.2063 $day^{-}1$	[7]
Implant with Porous Separator	-	-
Diffiusivity (D_i)	$6.0 \times 10^{-}6 cm^2/s$	[20]
Rectangular Shape, radius	0.10 cm	[11]
Rectangular Shape, width	0.70 mm	n/a
Separator, width	0.045 mm	n/a
Separator, pore size (d)	0.008-2.0 mm	n/a

the diffusion equations to reflect the convective drug transfer. We, therefore, focused on the diffusion and convection of IgG1 Fab drug doses to the posterior layers.

Diffusion flow model for the IgG1 Fab drug

The porous media flow in the posterior layers is assumed to be incompressible, and is governed by the following Darcy flow equation:

$$\vec{v} = -\frac{k}{\mu} \times \nabla p \tag{2.1}$$

where v, k, μ, and p are the flow velocity, the permeability of the medium, the viscosity, and the pressure of the fluid respectively. The permeability term in Dracy's law depends on the domain that we are studying and is different at different eye layers.

Diffusion-convection equations for the sclera, choroid, and retina layers

Drug diffusion through the layers of the posterior eye is modeled by the diffusion's First Law. As seen in Fig. 2.1.(b), the drug solution (IgG1 Fab) is released in the gel implant and delivered to the posterior eye. Molecular diffusion is deemed the main driving mechanism for drug transfer through the layers of the posterior eye. For calculating the transport of the drug through the layers of the posterior eye, we introduce the diffusion-convention equation in each layer of the posterior eye as follows: sclera (outer) layer:

$$\frac{\partial c_s}{\partial t} + \nabla^2 c + \vec{v} \cdot \nabla c = 0 \tag{2.2}$$

choroid (middle) layer:

$$\frac{\partial c_c}{\partial t} + \nabla^2 c + \vec{v} \cdot \nabla c = 0 \tag{2.3}$$

retina (inner) layer:

$$\frac{\partial c_r}{\partial t} + \nabla^2 c + \vec{v} \cdot \nabla c = 0 \tag{2.4}$$

In Eqs. (2)-(4), D_s, D_c, and D_r are the drug diffusivities in the sclera, choroid and retina layers, respectively, and $k_e c$ and $k_e r$ are rate constants of drug elimination due to the absorption to the veins in the choroid and retina, respectively. There is no drug elimination in the sclera and thus there is no rate constant of drug elimination in Eq. (2).

2.3 Validation: Drug delivery via hydrogel implant

IgG1 Fab is a macromolecular anti-VEGF drug routinely used to treat AMD. Experimental data on IgG1 Fab drug concentration in the layers of the posterior eye for intravitreal (IVT) injection or delivery from a local implant is not currently available. Clinical studies have shown that the therapeutic effects of drug doses of 0.5 and 1 mg/cm^3, regularly delivered by IVT injection, extend for two months [17]. In this section, we validate our simulation with independently reported data [11] for the delivery of IgG1 Fab to the layers of the posterior eye using a hydrogel implant (Fig. 2.2.(a)). Then we simulate the episcleral delivery of IgG1 Fab drug to the layers of the posterior eye via a new type of porous implant (Fig. 2.2(b)). The parameters used in the simulations for the transport of the IgG1 Fab fragment are in Table 1.

To validate our computational modeling with previous experimental and computational studies [11,16], we placed the IgG1 Fab drug source on the left inner wall of a hydrogel implant, as seen in Fig. 2.2.(a), to study drug delivery to the posterior layers. On the implant inner wall, the drug concentration is set to decay exponentially for 2 days of release as seen in Fig. 2.2.(b). We focus on the drug delivery across the posterior layers in terms of the time evolution of the drug concentration and drug delivery velocity across the layers. Fig. 2.3.(a) shows the time evolution of the average IgG1 Fab drug concentration in the sclera (black), choroid (red), and retina (blue) layers within two months after administration begins, for a monthly dose, $C_o = 1mg/cm^3$. Drug concentrations have been normalized with the therapeutic concentration value of Ctherapeutic = 150 mg/cm^3 [11]. This therapeutic concentration is the minimum required concentration of the drug that must exist to have an effective treatment. The corresponding solid symbols are computational results from a previous study [11]. Because of the very high amount of the initial drug concentration at the implant, there is a high value of drug concentration at the beginning, in the three different layers (Fig. 2.3.(a)). By the time the drug source weakens and the drug absorption overpowers the drug transfer from the implant, the concentration shows a decline. The velocity

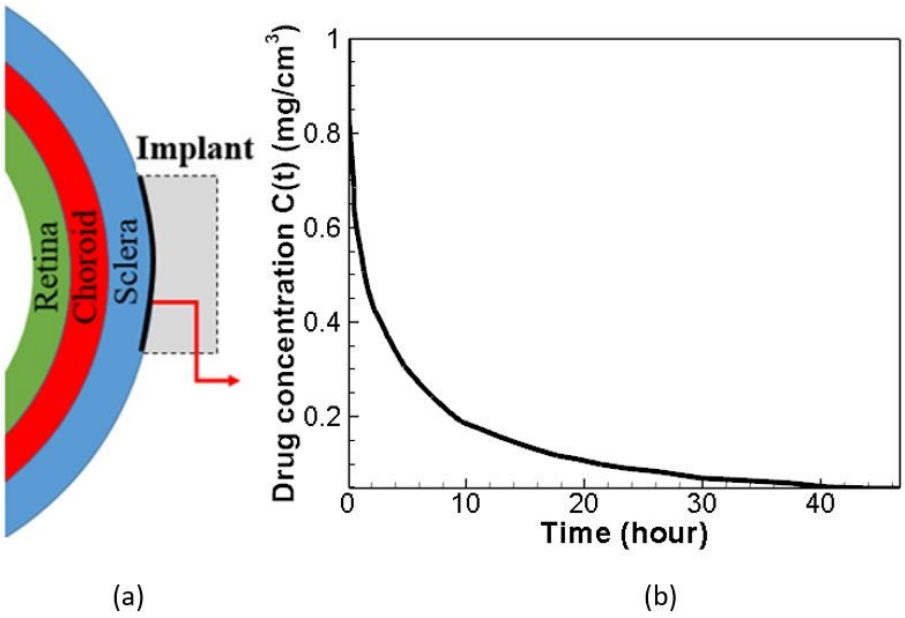

Fig. 2.2. The setup of IgG1 Fab drug in a hydrogel implant. Illustrations show (a) the drug source is placed on the hydrogel implant-sclera interface (black line) and (b) the exponential decay of the drug concentration at the implant when $C(t=0) = C_o = 1mg/cm^3$ [16]

profile along the choroid-sclera interface is shown in Fig. 2.3(b). The rapid change of the velocity at the beginning and the end of the graph can be attributed to the fact that there is a sharp pressure gradient between the outer surface of the sclera and the hyaloid membrane and the measurement starts to close the intersection of the sclera and the hyaloid membrane. The pressure gradient is uniform through the rest of our arc because the distance between retina's outer surface and sclera's outer surface remains the same. Overall, our simulation results agree well with the open data (Kavousanakis et al. 2014).

2.4 Numerical Results and Discussion

In this section, we investigated the effects of implant setup and implant structure on the drug delivery. We studied the role of drug source location on the concentration levels calculated in the posterior eye layers. Then, we conducted simulations of the

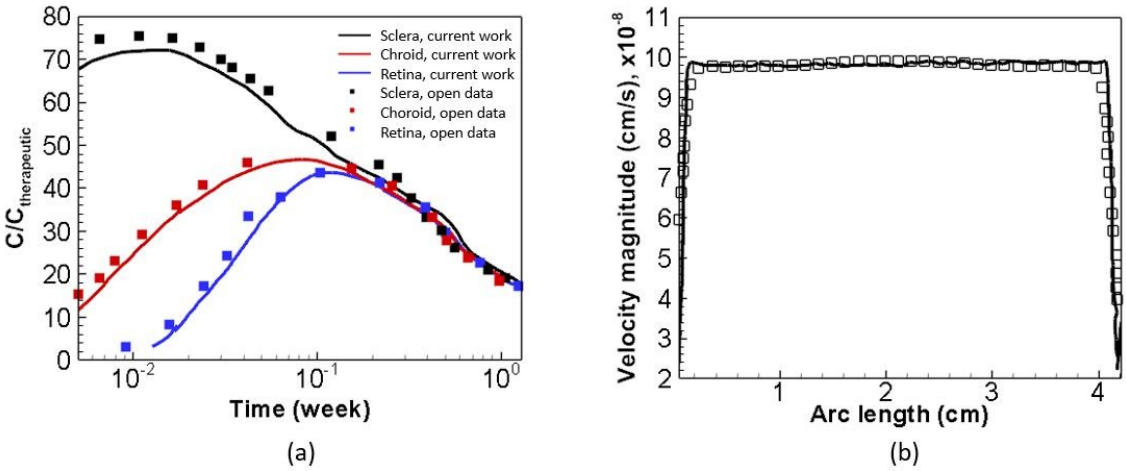

Fig. 2.3. Validation results regarding drug delivery to the posterior layers. Calculations show (a) time evolution of the average IgG1 Fab drug concentration in the sclera (black), choroid (red), and retina (blue) layers respectively. Solid lines are the results of the current simulations and solid squares are data from a previous study [11]. The velocity profile (b) along the choroid-sclera shows agreement with prior findings by [11]. The solid line is from the current simulation and the open squares are from reported open data reported by [11]

.

delivery of IgG1 Fab to the posterior layers using a porous implant. In this case, we analyzed the effect of pore size on drug concentration evolution and compared results against the former standard hydrogel implant. All these results and analysis are described next.

2.4.1 Role of drug source location

The previous study placed the drug on the left inner wall of the implant, Fig. 2.4.(a), which has eliminated the functionality of the implant. Here we explore the effect of drug source location in the implant on the drug delivery in the posterior eye layers. Fig. 2.4. shows the time evolution of the IgG1 Fab drug concentration in the three posterior layers using two different drug source locations in the implant: (a) left wall and (b) right wall. It is evident from these results that the location

of the drug source (i.e. concentration boundary condition) is important to consider in the evolution of the mean drug concentration. Placing the drug source in the sclera-implant interface (case (a)) was found to be more accurate when comparing data against prior simulations [11] than the alternative (case (b)). This despite the fact our implant dimensions are smaller than those reported before by [11] yet the concentration levels and trends are similar as demonstrated in Fig. 2.4.(a). It is reasonable to expect drug concentration levels in the eye layers to be higher in case (a) than in case (b) - where drug transport will require more time to reach all three layers and thus concentration levels will decrease. Note also that case (a) has an enlarged sclera-implant interface (i.e. length of black line) compared to case (b) and hence the higher values.

Furthermore, as seen in Fig. 2.4, the drug concentration curves show higher peaks for case (a) than case (b) in all three layers. This can be attributed to the fact that drug spreads into the eye faster than it gets eliminated, and concentration peaks are higher since the drug source is closer to the eye layers or in "direct contact with the sclera". However, the drug source will change location (case (b)), for an implant containing a porous separator as in Fig. 2.4.(a), which will essentially create a diffusion barrier to drug transport and further slowdown drug diffusion.

2.4.2 Diffusion through porous implants: Pore size effect

The objective of the current research is to explore a new implant with porous media structure that can efficiently control the drug delivery in the posterior eye. In this study, we introduce a single separator in the implant to mimic the porosity of a porous media structure, as seen in Fig. 2.5.(a), and study the effects of the separator traits (i.e. pore size) on the drug delivery. The physical properties of this implant are the same as the physical properties of the sclera (i.e. diffusion coefficient and permeability). As shown in Fig. 2.2.(a), the drug is placed on the right inner wall of the implant with the same concentration decay as in Fig. 2.2.(b).

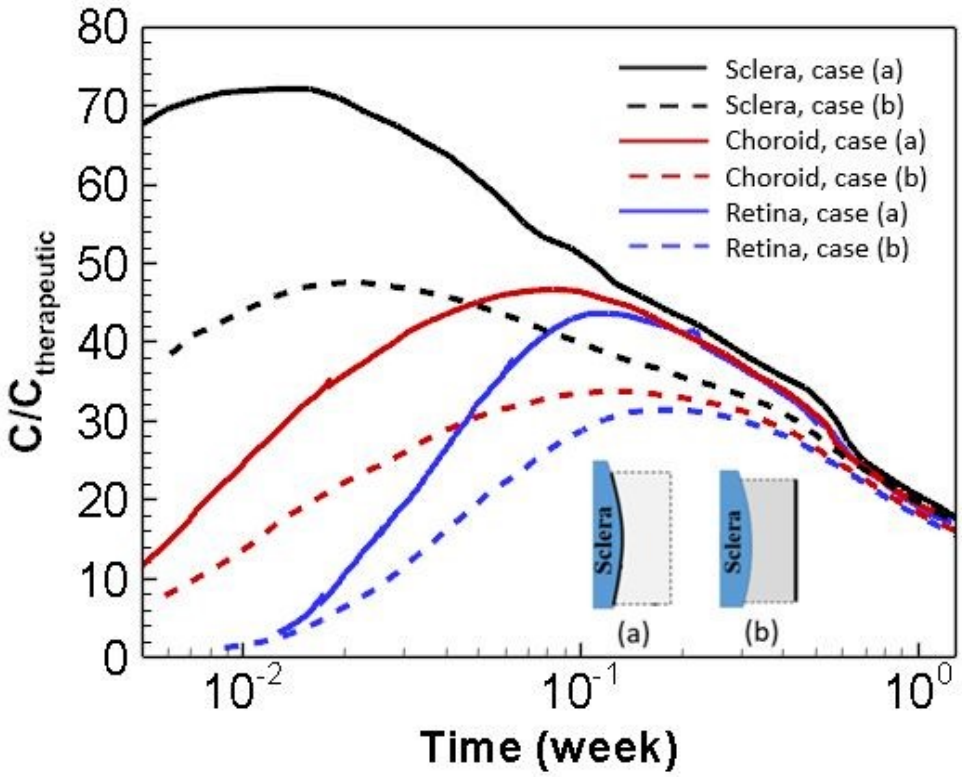

Fig. 2.4. Time evolution of the average IgG1 Fab drug concentration in the sclera (black), choroid (red), and retina (blue) layers, during the first two months after administration begins. The drug sources are placed on the (a) left wall (case a) and (b) right wall (case b) of the implant.

The pore arrangement is adjustable thus the drug release to the posterior layers can be precisely controlled through the porosity of the porous media structure The concept of introducing porous barriers (separators) within an implant is used in this study to examine the effect of porosity on drug release. Since the drug source (concentration boundary condition) is placed on the right side of the porous implant as in Fig. 2.5.(b), this allows the evaluation of pore sizes inside the implant for sustained drug delivery in a systematic manner.

We have used different pore diameters in a separator inside a hydrogel implant (Fig. 2.5.(a)) to examine their effect on drug concentration to the posterior eye layers. Clinical studies with IgG1 Fab, delivered by IVT injection, have reported that

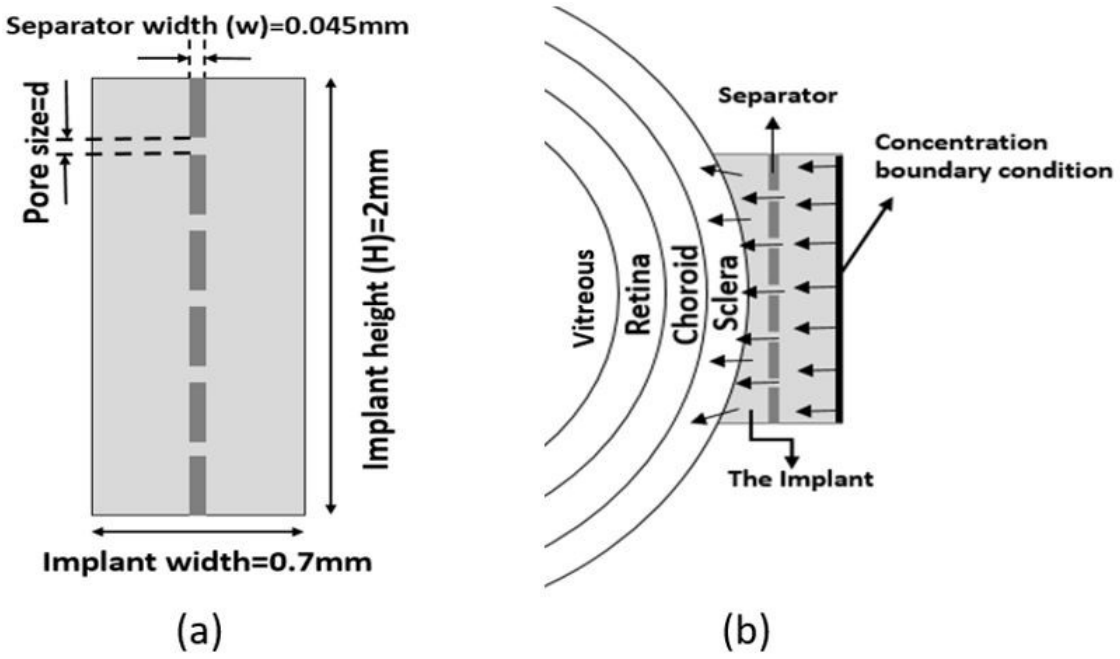

Fig. 2.5. Illustration of the porous implant structure comprising of a single separator with adjustable pore size. The diagrams show (a) key dimensions of the implant and (b) implant position next to the sclera, arrows indicating drug flow towards posterior layers. In this study, the IgG1 Fab drug source location is placed on the right inner wall of the implant.

the time during which the drug concentration in the choroid and retina layers is at a therapeutic level is about 8 weeks. Fig. 2.6. summarizes the evolution of drug concentration in each of the eye layers (sclera, choroid, and retina) as a function of pore diameter during this period of interest. Drug concentrations have been normalized with the therapeutic concentration ($C_{therapeutic} = 150\mu g/l = 150mg/cm^3$), which completely inhibits neovascularization. As Fig. 2.6. shows, the average drug concentrations in the sclera (a) remains higher at all times compared to those in the choroid (b) and the retina (c). This can be attributed to the fact that the released drug in the latter (b) and (c) has to pass through the implant and larger sclera, diffusing at a lower speed into the eye due to differences in diffusivity values and drug elimination rates. Results in Fig. 2.4. indicate that the average drug concentration levels in all

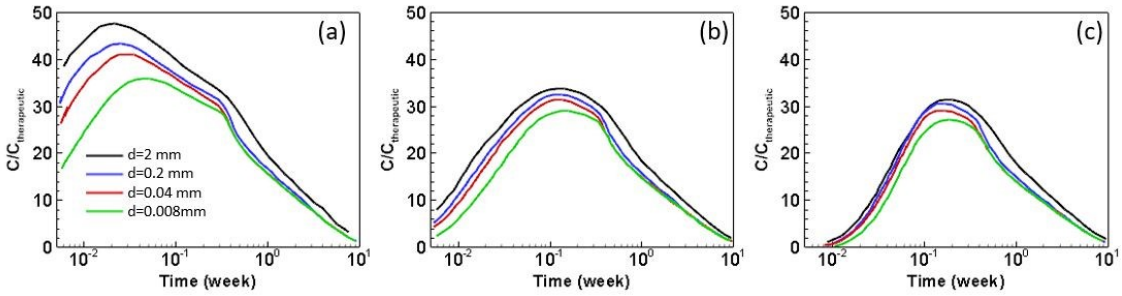

Fig. 2.6. Average drug concentration in the (a) sclera, (b) choroid and (c) retina using a porous implant, as a function of pore sizes as shown in Fig. 2.6.(a), during the first two months after administration begins and where $c_o = 1mg/cm^3$. Legend denotes pore size vary in diameter d in case: 2, 0.2, 0.04 and 0.008 mm.

three layers are lower for the porous implant Fig. 2.4.(b) than those for the standard hydrogel implant in Fig. 2.4.(a). The porous separator is essentially a barrier to drug diffusion and thus drug concentration levels are expected to diminish. The trends in Fig. 2.6. (a-c) show all drug concentration curves increase at the beginning until they reach a maximum value (peak) before decreasing rapidly for all pore sizes. The differences in drug concentrations in Fig. 2.6. (a-c) can be explained as follows. It will likely take more time for the drug to diffuse through the porous implant (than the standard implant) and reach all three layers, and given the different diffusivities per layer, the average drug concentrations would be lower in each subsequent inner layer (i.e. sclera > choroid > retina with the lowest drug concentrations) as seen in Fig. 2.6. (a-c).

More significantly, results in Fig. 2.6. show that as pore size decreases in the porous implant so do the average drug concentration levels in all three layers. Fig. 2.6. suggests a correlation between pore size and drug concentration, i.e. the smaller the pore diameter is, the lower the average drug concentration is in each layer and vice versa. The average drug concentration profiles reveal distinct peaks in the layers, in particular in the sclera (Fig. 2.6.(a)). It is noteworthy that as pore diameter shrinks, the drug diffuses through the porous implant into the sclera faster (Fig. 2.6.(a)).

2.5 Conclusion

To study the effects of the implant structure on the drug delivery to the posterior eye, we use a representative model of human eye together with an implant attaching on the sclera layer on the back. Fig. 2.1.(b) shows the schematic of a cross-sectional view of the posterior segment of a human eye (dimensions are not scaled). The vitreous humor is a gel-like porous medium, which comprises most of the interior eye. It is enclosed by the retina layer on the posterior eye and by the lens and hyaloid membrane on the front side of the eye. The implant is attached to the posterior eye close to the optic nerve and it is used to release the drug during an eye treatment. The front side of the eye, i.e. lens and pupil, were not be taken into account because they are almost impermeable to drugs as there is constant flow drainage between the iris and the lens which washes any drug away, and thus can be eliminated.

3. LATTICE BOLTZMANN METHOD AND WALL SHEAR STRESS SIMULATION

3.1 Introduction to Lattice Boltzmann Method

In the past few decades, by the growth of computer powers, scientists have started to use CFD more than ever. In thermo-fluid science, we generally have to deal with phenomenons that consist of highly non-linear partial differential equations (PDEs). A great example of such a comparison is the well-known Navier-Stokes equations. The Navier-Stokes equations contain highly non-linear convective terms and are highly coupled. To this day, there is no analytical solution for the general format of Navier-Stokes equations. The analytical solution of NS is one of the great problems of the century. The most popular way to deal with these equations is to use computational methods. There are many ways developed to solve the Navier-Stokes equations numerically. Perhaps the most famous routines in solving the NS equations (and also the most fundamental) are the finite difference method (FDM) and finite volume method (FVM). We use a set of rectangular grids in the finite difference method and discrete the governing equations over those grids. In each cell, the cell's information is located in the middle. The governing equations are discretized over the cells and solved numerically using the values at the center of the cell. The finite volume method is a more complex, however, more accurate way. It uses the divergence theorem to transform the volume integral of PDEs into the surface integral to transfer the flow of information from each cell to another. The NS equations are derived with the assumption of continuum macroscopic space. In recent years scientists have used a different approach to solve the CFD problems called the lattice Boltzmann method (LBM). The LBM has become a popular and alternate method in many CFD-related fields, such as flow in porous media and heat transfer problems [21]. In this approach,

we do not use the familiar Navier-Stokes equations. Instead, we change our sight to the kinetic theory equations and use the distribution function to solve the kinetic theory equations. Although LBM does not use the Navier-Stokes equations, we use the macroscopic parameters similar in Navier-Stokes, such as velocity, density, and pressure, to solve the field equations. Perhaps the most popular method in solving the LBM is solving the lattice Boltzmann equations using the linear collision operator provided by Bhatnagar–Gross–Krook [22].

The origins of the LBM returns to the lattice-gas-automata (LGA) [23]. In this method, the lattice has n-dimensions and is regular; the gas takes the direction of the lattice, and automata shows that the gas has to obey the collision process while obeying a specific function. The problem with this method was the small natural oscillations in the results, the dependence of the velocity to the pressure, and the large dissipation in the numerical solution [24]. Later, by the means of a hexagonal lattice, the Navier-Stokes equations were recovered. The problem of the noise oscillations was solved later by the usage of the Boolean operator [25]. Higuera and Jimenez proposed a linearized collision operator and assumed that the distribution function is close to the equilibrium function locally [26].

The linearized collision operator Bhatnagar–Gross–Krook (BGK) has been used more frequently by researchers and perhaps is the most famous one. In this collision operator, boundary conditions play an essential role. The boundary condition is different from the well-known boundary conditions that we use in the finite volume method in CFD. In lattice Boltzmann, we deal with the collision of the particles, and the fact that the boundary conditions are determined based on the collisions. The bounce-back boundary condition is famous in LBM. Its origins get back to the LGA and is used in most of LBM simulations. We will explore this in the kinetic theory and mention why this boundary condition is used in section 3.1.1. In this boundary condition, the distribution function before and after the collision has the opposite direction.

It is crucial to be able to recover the Navier-Stokes equations from the Boltzmann equations, and indeed there have been many types of research conducted to obtain the relation between lattice Boltzmann equations (LBE) and Navier-Stokes (NS) equations [27–30]. The LBE uses the collision operator to describe the interaction between the particles. One advantage of the LBE over the NS equations is the gaseous flows [31]. LBE equations make it easier to study the gaseous flows in a broader range of flow regimes. However, it is still uncommon to use the LBE equations in the study of the flows due to the complexity of the collision parameters and the unfamiliar concept of kinetic theory between the researchers in fluid dynamics.

The common notation in LBM is as D_xQ_y in which x stands for the dimensions and y stands for the number of the velocity direction that particles have. For example, D_1Q_2 shows a system with one dimension and two velocities vectors. It is fruitful to point at some differences between Navier-Stokes equations and LBE:

- The Navier-Stokes equations use second-order partial differential equations, but the kinetic equations used in LBM have the first order of magnitude accuracy.
- The convective term in Navier-Stokes equations are non-linear but the convective term in LBE is linear.
- The Navier-Stokes equation uses the iterative method, but the LBM method does not.
- The boundary conditions in LBM studies the bounce back of the particles, while in Navier-Stokes equations is about the macroscopic parameters. .

We will narrow down our focus to the incompressible fluids to simplify the mathematical procedure. The flow in biomedical engineering applications is highly considered to be incompressible, therefore the incompressible flow assumption will not reduce the accuracy of our model. Mach number is a useful parameter to draw a line between compressible and incompressible fluid.

$$Ma = \frac{u_0}{c_s} \tag{3.1}$$

The u_0 is the velocity of the fluid, and c_s is the speed of the sound.

To maintain the incompressible fluid flow condition in our computation, we accept the famous criteria for describing incompressible fluids:

$$Ma<0.3 \tag{3.2}$$

The fluid dynamic can be sub-categorized into three levels [32]: (i) Molecular Dynamics: This considers each molecule's motion. The position and velocity of each molecule are studied in Molecular Dynamics. These systems contain a large number of molecules, and the behavior of the system can be studied by tracking every molecule's trajectory in the system. (ii) Kinetic Theory: which uses the means of statistical thermodynamics. It uses distribution functions to describe the system. (iii) Hydrodynamics: studies the fluid structure at a macroscopic level. The individual motion of each molecule is not an essential factor at this level, and the bulk motion of the fluid is the only important issue in it. The conservation laws and continuum fluid dynamic laws lay in this level. Parameters such as velocity ($\vec{u}$), density (ρ), pressure (p), temperature (T) etc are measured in macroscopic level. These variables represent the average behavior of a large number of molecules in an element. All well-known equations such as Navier-Stokes equations, energy equation lay at this level. The kinetic theory can be seen as a bridge between molecular dynamics and hydrodynamics.

How to classify a system as one of the three mentioned systems? In order to study a system of molecules, it is necessary to determine whether the motion of every single molecule is essential or not. In a lot of cases, this can be assessed without much effort. In studying a wind turbine, we usually use coarse approximations and analyze a large volume of the system. In many cases, the problem requires us to consider small volumes of fluid and, thus, a smaller number of molecules in the volume. There must be a parameter to let us characterize the fluid in one of the mentioned categories.

The Knudsen number, defined as $K_n = \lambda/L$, is a criteria for categorizing a system of molecules. Here, L is the characteristic dimension of the system of particles, andλ is the mean free path of the molecules. Continuum models based on NS equations and Euler equations are generally valid when $5 \geq K_n \geq 0.01$, but can be extended into the slip-flow regime ($0.1 \geq$K$_n \geq 0.01$) by appropriate treatment of the wall boundary. However, the discrete particle model based on the Boltzmann equation governs almost all the flow regimes ($K_n \leq 100$). This implies the fact that Boltzmann equations can cover a wide range of applications in fluid flow problems.

3.1.1 Kinetic theory

Although the fluid flow problems are generally described by Navier-Stokes equations and the rules of the continuum system, it indeed is formed from a large number of molecules. Thus it can be described with kinetic theory. The fundamental assumptions in kinetic theory are:

- The mean free path of the molecule is much bigger than the molecule size.
- The system contains molecules that move incessantly with a distribution.
- The collisions between molecules are elastic and contain no exerted force.
- The Newtonian laws of motion are applicable.

According to the mentioned bullet-points, Newton's laws are applied in kinetic theory, and at the same time, we have a relatively large number of molecules. Thankfully we do not need to solve every single molecule equation of motion. We are using the macroscopic parameters such as velocity, density, and temperature to represent the average bulk behavior of molecules. The next step to study the system is to find a distribution that describes these parameters the best.

3.1.2 Boltzmann equation

Let's assume $x_i(or\vec{x})$ as the Cartesian coordinates of a physical space, and $\xi_i(or\vec{\xi})$ the molecular velocity. Our goal is to determine a distribution function $f(\vec{x},\xi,t)$, for the velocity in which determines the probability of finding a molecule with velocity $\vec{x_i}$, at position $\vec{x}$ and time t. This distribution function is the key to find other parameters such as $\rho(\vec{x},t)$, the momentum density $\vec{u}(\vec{x},t)$, the internal energy density $e(\vec{x},t)$, the stress tensor $\sigma(\vec{x},t)$, and the heat flux vector $\vec{q}(\vec{x},t)$ can be obtained by using the following equations:

$$\rho(\vec{x},t) = \int f(\vec{x},\xi,t)d\vec{\xi} \tag{3.3}$$

$$\rho\vec{u}(\vec{x},t) = \int \vec{\xi} f(\vec{x},\xi,t)d\vec{\xi} \tag{3.4}$$

$$\rho e(\vec{x},t) = 1/2 \int \vec{\xi_0}^2 f(\vec{x},\xi,t)d\vec{\xi} \tag{3.5}$$

$$\sigma(\vec{x},t) = -\int \vec{\xi_0}\vec{\xi_0} f(\vec{x},\xi,t)d\vec{\xi} \tag{3.6}$$

$$\vec{q}(\vec{x},t) = 1/2 \int \vec{\xi_0}(\vec{\xi_0}\cdot\vec{\xi_0}) f(\vec{x},\xi,t)d\vec{\xi} \tag{3.7}$$

Where $\vec{\xi_0} = \vec{\xi} - \vec{u}$, is the molecule velocity respect to the bulk velocity of the flow. One of the principles in kinetic theory gives us the following relation between energy density and temperature:

$$e = \frac{D_0}{2RT} = \frac{D_0}{(2m)k_BT} \tag{3.8}$$

where D_0 is the degree of freedom of each molecule, and m is the mass of a single molecule. R and k_B are the ideal gas constant and Boltzmann constant, respectively. The degree of freedom coefficient depends on the number of atoms in the molecule. For multi-atomic molecules, it is indeed a challenge to find this coefficient, but for this case, we are going to study the single-atomic gas molecules in which $D_0 = 3$. The governing equations of the kinetic theory are all a product of the distribution function $f(\vec{x},\xi,t)$. The famous lattice Boltzmann equation is:

$$\frac{\partial f}{\partial t} + \xi_i \frac{\partial f}{\partial x_i} = J(f) \tag{3.9}$$

Where $J(f)$ is a function that describes the distribution function change due to the collisions. As it was mentioned, the collisions are elastic and conservative and can be shown as:

$$\int d\vec{\xi} J(f) \begin{bmatrix} 1 \\ \vec{\xi} \\ \xi^2 \end{bmatrix} = 0 \tag{3.10}$$

3.1.3 Collision term and its property

The first step to solve the equation 3.9 is to derive an equation for the collision parameter $J(f)$. To get an expression about the collision parameter, we are going to take the following assumptions:

- We only take into account the binary collision.
- The collisions happen in a short range.

The other assumption is the Boltzmann gas limit [33]:

$$N \longrightarrow \infty$$
$$m \longrightarrow 0$$
$$\nu \longrightarrow 0$$
$$N\sigma^2 \longrightarrow constant$$
$$Nm \longrightarrow constant$$

In which N is the total number of molecules, m is the molecular weight and the ν is a characteristic force length. We finally can get the collision function as [34]:

$$J(f) = \frac{1}{m} \int dS d\vec{\xi_1} \mid \vec{\xi_1} - \vec{\xi} \mid (f' f_1' - f f_1) \tag{3.11}$$

In which dS is the cross section of the collision. $\vec{\xi'}$ and $\vec{\xi_1'}$ are the velocities of the molecules before the collision, and $\vec{\xi}$ and $\vec{\xi_1}$ are the molecular velocities after the collision.

We can show the collision formula in another format. It is shown that the collision term can be rearranged in the following form due to the symmetrical behavior [34].

$$\int d\vec{\xi} J(f)\psi(\vec{\xi}) = \frac{1}{m}\int dS d\vec{\xi_1} d\vec{\xi} \mid \vec{\xi_1} - \vec{\xi} \mid (f'f_1' - ff_1)\psi(\vec{\xi}) \tag{3.12}$$

In which $\psi(\vec{\xi})$ is a function of $\vec{\xi}$. We can simply replace the $\vec{\xi}$ in $\psi(\vec{\xi})$ with $\vec{\xi_1}$ on the right hand side of the equation:

$$\int d\vec{\xi} J(f)\psi(\vec{\xi}) = \frac{1}{m}\int dS d\vec{\xi_1} d\vec{\xi} \mid \vec{\xi_1} - \vec{\xi} \mid (f'f_1' - ff_1)\psi(\vec{\xi_1}) \tag{3.13}$$

By substituting the variables $\vec{\xi'}$ and $\vec{\xi_1'}$ with variables $\vec{\xi}$, $\vec{\xi_1}$ and some mathematical simplifications, we can transform $\vec{\xi}$, $\vec{\xi_1}$ to $\vec{\xi'}$ and $\vec{\xi_1'}$:

$$\begin{aligned}\int d\vec{\xi} J(f)\psi(\vec{\xi}) = -\frac{1}{m}\int dS d\vec{\xi_1'} d\vec{\xi'} \mid \vec{\xi_1} - \vec{\xi} \mid (f'f_1' - ff_1)\psi(\vec{\xi'}) = \\ -\frac{1}{m}\int dS d\vec{\xi_1} d\vec{\xi} \mid \vec{\xi_1} - \vec{\xi} \mid (f'f_1' - ff_1)\psi(\vec{\xi'})\end{aligned} \tag{3.14}$$

Similarly,

$$\int d\vec{\xi} J(f)\psi(\vec{\xi}) = -\frac{1}{m}\int dS d\vec{\xi_1} d\vec{\xi} \mid \vec{\xi_1} - \vec{\xi} \mid (f'f_1' - ff_1)\psi(\vec{\xi_1'}) \tag{3.15}$$

By using the 3.14 and 3.15 the new combination would be:

$$\begin{aligned}\int d\vec{\xi} J(f)\psi(\vec{\xi}) = -\frac{1}{4m}\int dS d\vec{\xi_1} d\vec{\xi} \mid \vec{\xi_1} - \vec{\xi} \mid [\psi(\vec{\xi}) + \psi(\vec{\xi_1}) - \psi(\vec{\xi'}) - \psi(\vec{\xi_1'})] = \\ \frac{1}{4}\int d\vec{\xi_1} d\vec{\xi} J(f)[\psi(\vec{\xi}) + \psi(\vec{\xi_1}) - \psi(\vec{\xi'}) - \psi(\vec{\xi_1'})]\end{aligned} \tag{3.16}$$

We can use this equation to obtain a new form of the collision equation as:

$$\int d\vec{\xi} J(f) \begin{bmatrix} 1 \\ \vec{\xi} \\ \xi^2 \end{bmatrix} = \frac{1}{4}\int d\vec{\xi} J(f) \begin{bmatrix} 1+1-1-1 \\ \vec{\xi}+\vec{\xi_1}-\vec{\xi'}-\vec{\xi_1'} \\ \xi^2+\xi_1^2-\xi'^2-\xi_1'^2 \end{bmatrix} = 0 \tag{3.17}$$

These are a set of three individual equations: The conservation of mass, the conservation of momentum, and the conservation of energy, respectively. The zero value at the right-hand side of the equation implies the fact that our equations are conservative.

We formerly have assumed that the collisions are between two particles. It means that if $\psi(\vec{\xi})$ equals to one, then in a binary collision, ξ, and ξ^2 corresponding to mass density, momentum, and energy density.

3.1.4 H-theorem and Equilibrium equations

All the isolated system will finally meet the equilibrium if they are given enough time. Consider the H function as the following:

$$H(\vec{x},t) = \int f \ln f d\vec{\xi} \tag{3.18}$$

by taking a derivative from equation 3.18 we have:

$$\frac{\partial H}{\partial t} = \int (1+\ln f)\frac{\partial f}{\partial t} d\vec{\xi} \tag{3.19}$$

If we only consider a spatially uniform system, i.e., f depends on t only, the above equation can be written as:

$$\frac{\partial H}{\partial t} = \int (1+\ln f) J(f) d\vec{\xi} \tag{3.20}$$

we assume that the f only is a function of t; therefore, the equation can be written as:

$$\frac{\partial H}{\partial t} = \int dS d\vec{\xi_1} d\vec{\xi} \mid \vec{\xi_1} - \vec{\xi} \mid (f' f_1' - f f_1)\psi(\vec{\xi'}) \ln(\frac{f f_1}{f' f_1'}) \tag{3.21}$$

With the combination of the Boltzmann equation and the collision operator. Since

$$\mid \vec{\xi_1} - \vec{\xi} \mid (f' f_1' - f f_1)\psi(\vec{\xi'}) \ln(\frac{f f_1}{f' f_1'}) < 0 \tag{3.22}$$

and all the other terms in the above equation are positive, as a result:

$$\frac{\partial H}{\partial t}<0 \tag{3.23}$$

The slope of this function is always less than zero, which tells us that the H function always decreases with time. This is known as the Boltzmann's H-theorem. As it was mentioned, the studied H-theorem is only a function of t. The reader can refer to [33] for more information about the non-uniform systems. By combining the equations 3.19 and 3.23 we can obtain a new form of equation for the equilibrium:

$$f f_1 = f' f_1' \tag{3.24}$$

By taking a logarithm from the equation 3.24 we have another form as:

$$\ln f + \ln f_1 = \ln f' + \ln f_1' \tag{3.25}$$

we can conclude that the previous equation can lead us to the following expression:

$$\ln f_M(\vec{\xi}) = A + \vec{B} \cdot \xi + C\xi^2 \tag{3.26}$$

The five constants A, B_1, B_2, B_3, and C above are not arbitrary since we have an equal number of constraints relating the first five moments given in Eqs. 3.3-3.7. The resulting unique value of f obtained for the equilibrium state is:

$$f_M(\vec{\xi}) = (\frac{\rho}{2\pi RT^{3/2}})e^{-}(\vec{\xi} - \vec{u})^{2/2RT} \tag{3.27}$$

which is the well-known Maxwell-Boltzmann equation.

3.1.5 Moments equations

We can integrate equation 3.9 with respect to velocity ψ and obtain the moment equations. The results will be the conservation of mass and momentum and the conservation of energy equations. By taking the zeroth-order moment of the Boltzmann equation, we have:

$$\frac{\partial}{\partial t}\int f d\vec{\xi} + \nabla \cdot \int \vec{\xi} f d\vec{\xi} = \int J(f) d\vec{\xi} = 0 \tag{3.28}$$

which gives us:

$$\frac{\partial \rho}{\partial t} + \nabla \cdot (\rho \vec{u}) = 0 \tag{3.29}$$

Which is the famous continuity equation. Using equation 3.9, the first-order moment of the Boltzmann equation is:

$$\frac{\partial}{\partial t}\int \vec{\xi} f d\vec{\xi} + \nabla \cdot \int \vec{\xi}\vec{\xi} f d\vec{\xi} = \int \vec{\xi} J(f) d\vec{\xi} = 0 \tag{3.30}$$

The term $\int \vec{\xi_0} f d\vec{\xi} = 0$ and therefore, we can write the LHS of the equation as follows:

$$\nabla \cdot \int (\vec{\xi_0} + \vec{u})(\vec{\xi_0} + \vec{u}) f d\vec{\xi} = \nabla \cdot [\rho(\vec{u}\vec{u}) + \int \vec{\xi_0}\vec{\xi_0} f d\xi] \tag{3.31}$$

By substituting equation 3.31 into equation 3.28, we obtain:

$$\frac{\partial \vec{u}}{\partial t} = -(\vec{u} \cdot \nabla)\vec{u} - \frac{1}{\rho}\nabla \cdot \int \vec{\xi_0}\vec{\xi_0} f d\vec{\xi} \tag{3.32}$$

Which is the famous momentum or Navier-Stokes equation. The second order of moment equation is:

$$\frac{1}{2}\frac{\partial}{\partial t}\int \xi^2 f d\vec{\xi} + \frac{1}{2}\nabla \cdot \int (\xi)^2 \vec{\xi} f d\vec{\xi} = \frac{1}{2}\int \xi^2 J(f) d\vec{\xi} = 0 \tag{3.33}$$

we can simplify the left term of the LHS of equation as following:

$$\frac{\partial}{\partial t}(\frac{1}{2}\int (\vec{\xi_0} + \vec{u})^2 f d\vec{\xi}) = \frac{\partial}{\partial t}[\int \xi^2 + u^2) f d\vec{\xi}] = \frac{\partial}{\partial t}(\frac{1}{2}\rho u^2 + \rho\epsilon) \tag{3.34}$$

and the second term can be extended as:

$$\nabla \cdot \frac{1}{2}\int (\vec{\xi_0} + \vec{u})^2 (\vec{\xi_0} + \vec{u}) f d\vec{\xi} = \nabla \cdot [\rho\vec{u}(\frac{1}{2}u^2 + \epsilon) + \vec{u} \cdot \int \vec{\xi_0}\vec{\xi_0} f d\xi + \frac{1}{2}\int \vec{\xi_0}\xi_0^2 d\vec{\xi}]$$

Thus we can rewrite the final equation as:

$$\frac{\partial \epsilon}{\partial t} = -\vec{u} \cdot \nabla\epsilon - \frac{1}{\rho}[\nabla \cdot (\vec{u} \cdot \int \vec{\xi_0}\vec{\xi_0} f d\vec{\xi} - \vec{u} \cdot \nabla \cdot \int \vec{\xi_0}\vec{\xi_0} f d\vec{\xi})] - \frac{1}{\rho}\int \frac{1}{2}\xi_0^2 \vec{\xi_0} f d\vec{\xi} \tag{3.36}$$

and by knowing the fact that $\epsilon = 3RT/2$,

3.1.6 Single relaxation time and BGK model

The frequent used collision parameter in LBM is the model given by Bhatnager, Gross, and Krook (BGK) [35]. The collision term in this method is:

$$J(f) = -Z(f - f_M) \tag{3.37}$$

where f_M is called the Maxwellian distribution function and Z is the mean collision frequency. We can write a new form of Boltzmann equation by substituting the collision term as:

$$\frac{\partial f}{\partial t} + \xi_i \frac{\partial f}{\partial \xi_i} = -Z(f - f_M) \tag{3.38}$$

which is the lattice Boltzmann equation with BGK collision parameter. by using the Taylor series to expand the equation to the first order of magnitude 3.38 we will have the following form:

$$f(\vec{x} + \vec{\xi}\Delta t, \vec{\xi}, t + \Delta T) = \frac{1}{\tau}[f(\vec{x}, \vec{\xi}, t) - f_M(\vec{x}, \vec{\xi}, t)] \tag{3.39}$$

In which $\tau = \frac{1}{Z\Delta t}$ is the relaxation time and Δt is the time step. we go further and discrete the equation in phase space and consider the low Mach number assumption for the problem in which leads to the single-relaxation time lattice Boltzmann equation:

$$f_\alpha(\vec{x} + \vec{e_\alpha}\Delta t, t + \Delta t) - f_\alpha(\vec{x}, \vec{e_\alpha}t, t) = \frac{1}{\tau}[f_\alpha(\vec{x}, \vec{e_\alpha}t, t) - f_\alpha^{eq}(\vec{x}, \vec{e_\alpha}t, t) \tag{3.40}$$

$f_\alpha^{eq}(\vec{x}, \vec{e_\alpha}t, t)$ is the equilibrium function and the e_α is the lattice velocity. The only drawback with the BGK lattice Boltzmann collision operator is that it is valid for small Knudsen numbers ($k_n 0.1$). We can use more sophisticated collision operations to be able to deal with larger Knudsen numbers.

3.1.7 Volumetric lattice Boltzmann method

As we have mentioned, the LBM uses kinetic theory, and the kinetic theory's discrete equations are solved over time. The LBM method is a unique representation

of discretized Navier-Stokes equations up to the second of accuracy [20, 36]. In a conventional LBM method, everything is node-based. The particles are located at the lattice nodes. As time goes by, these particles collide with each other and stream to the nearby nodes toward their velocity directions. One celebrated LBE with the collision operator provided by Bhatnagar-Gross-Krook (BGK) can be written as [37]:

$$f_i(\vec{x} + \vec{e_i}\Delta t, t + \Delta t) = f_i(\vec{x}, t) + \Omega_i(\vec{x}, t) \tag{3.41}$$

$$\Omega_i(\vec{x}, t) = -\frac{f_i(\vec{x}, t) - f_i(\vec{x}, t)^{eq}}{\tau} \tag{3.42}$$

In which $\vec{e_i}$ is the velocity of the particle in the $i_t h$ direction, and is called the relaxation time. Generally, the bounce-back boundary condition works fine for many fluid flow problems in which the boundary is motionless. The scheme for moving boundary has been provided by [38]. In this method, the wall's velocity and its effect in studying the bounce-back of particles is also introduced. More sophisticated methods have been provided using the interpolation/extrapolation of velocity for complicated geometries and moving boundaries. Many of these methods do not deal well with the conservation of mass and momentum. This defect can cause further problems in balancing the particle distribution, and for complex geometries, this can lead to wrong results. Moreover, the usage of higher-order interpolation/extrapolation can cause a huge computational cost and at the same time is hard to implement. Aidun et. al. have come up with a method in which the mass transfer at the boundary is zero, but it also comes with its drawbacks [39]. One other way to meet the no-slip boundary condition at the wall is the diffusive bounce-back criteria [40]. In this scheme, we define a permeable boundary while applying the simple bounce-back of the particles. This method has gained high success in its accuracy in calculating a wide range of Reynolds numbers. Although all these progress has helped treat the boundary condition in LBM simulations, the major drawback is yet the interpolations at the boundaries. The interpolation increases the complexities of the problem and increases the computational cost dramatically and is especially hard to study moving boundaries.

The volumetric lattice Boltzmann method has originated from studying the moving boundaries [41]. In this method, we have an equal number of particles at each complete cell. At the boundary in which the solid wall cuts through the cell, the number of particles can vary. The amount of the solid wall that occupies the cell plays a vital role in this method. This can vary from zero (not occupied by the solid wall) to one (total solid space). One great advantage of the volumetric lattice Boltzmann method (VLBM) is that we can avoid using interpolations in the computations [37]. Several studies have been conducted to implement to increase the usage of a volumetric approach in LBM for complex boundaries. One efficient method. [42] used a cell-based velocity gradient revision and implemented bounce-back boundary conditions and could successfully simulate the flow in cylindrical geometry for below-average Reynolds numbers. They later provided a general VLBM algorithm and verified it [43]. Yu et. al. [44] have used the P-value parameter to show the ratio between the fluid and solid region. The equations in VLBM are derived based on the P-value parameter and will be used in this dissertation. We use the P_v to represent the P-value in the equations.

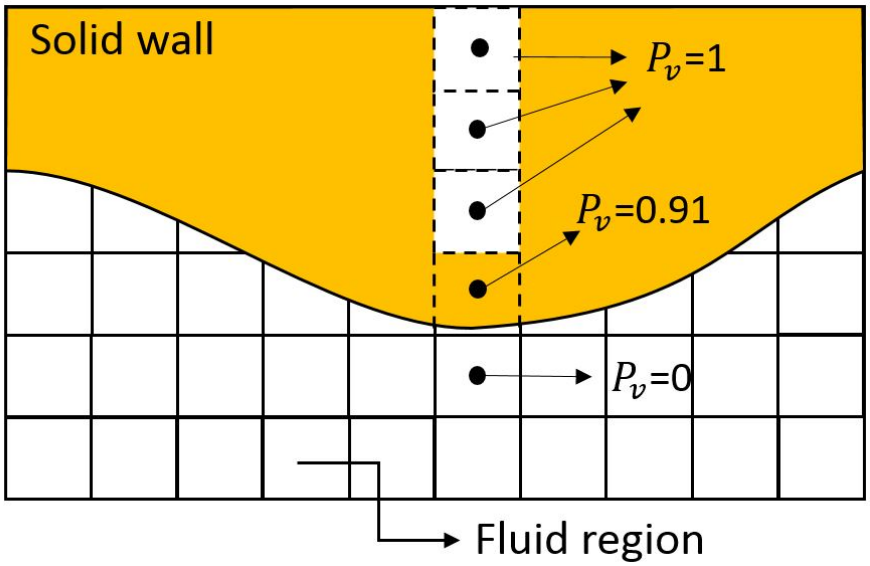

Fig. 3.1. The rectangular duct and attached coordination on it

The mathematical formulation for VLBM is almost the same for ordinary LBM equations. The only difference is the introduction of P-value into the equations. In the traditional LBM, the particles are located at lattice nodes, the same as Fig.3.2.(a) and can move toward the shown directions. For the VLBM, the particles are sitting at the lattice cells, as shown in Fig. 3.2.(b)

The function $n_i(\vec{x}, t)$ is the distribution of the particles that have the velocity $\vec{\xi_i}$ with the coordinate of $\vec{x}$ and at time t. Same as the ordinary LBM method, we can write the following equation:

$$n_i(\vec{x} + \vec{\xi}\Delta t, t + \Delta t) = n_i(\vec{x}, t) + \Omega_i(\vec{x}, t) \tag{3.43}$$

In which $\Omega_i(\vec{x}, t)$ is the described collision term. As we have mentioned, the boundary cells play an important role in the formulation of VLBM. It is important to have a mathematical

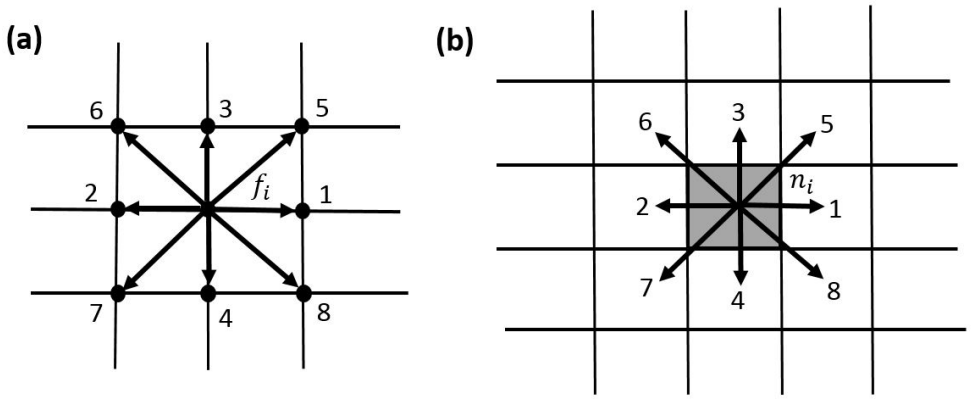

Fig. 3.2. The comparison of the node-based lattice and volume-based lattice in a D2Q9 setup.

representation of the P-value in order to use in VLBM. Consider ΔV_f as the volume of the fluid in a cell. We can use the amount of P_v to calculate the ΔV_f for every cell.

$$\Delta V_f = (1 - P_v(\vec{x}))\Delta V \tag{3.44}$$

Where ΔV is the volume of each cell. In the lattice unit, this volume equals unity. There is a slight difference between the particle density distribution in the conventional LBM f_i and VLBM n_i. They can be related with the help of fluid volume as:

$$f_i(\vec{x},t) = n_i(\vec{x},t)/\Delta V_f(\vec{x},t) \tag{3.45}$$

By using the BGK model and single time relaxation, we would have the following equation for the collision parameter:

$$\Omega_i(\vec{x},t) = -\frac{1}{\tau}[n_i(\vec{x},t) - n_i^{eq}(\vec{x},t)] \tag{3.46}$$

In which the particle distribution function can be written as:

$$n_i^{eq}(\vec{x},t) = N\omega_i[1 + \frac{\vec{\xi_i}\cdot U}{c_s^2} + \frac{(\vec{\xi_i}\cdot\vec{U})^2}{2c_s^4} - \frac{\vec{U}\cdot\vec{U}}{2c_s^2}] \tag{3.47}$$

In which the particle distribution function can be written as:where N is the number of the particles at each lattice cell:

$$N(\vec{x},t) = \sum_i n_i(\vec{x},t) \tag{3.48}$$

ω_i is the weight assigned to the velocity in the i_th direction and c_s si the speed of sound. The equations for density, velocity, and pressure are:

$$\rho(\vec{x},t) = \sum \frac{n_i(\vec{x},t)}{1 - P_v(\vec{x},t)} \tag{3.49}$$

$$\vec{u}(\vec{x},t) = \frac{\sum \xi_i n_i(\vec{x},t)}{\sum n_i(\vec{x},t)} \tag{3.50}$$

$$p(\vec{x},t) - p_0 = c_s^2[\rho(\vec{x},t) - \rho_0] \tag{3.51}$$

In which ρ_0 and p_0 are reference densities and pressures.

3.2 Study of Wall Shear Stress in pulsatile flows

3.2.1 Introduction to pulsatile flow

Pulsatile flow or Womersley flow is a flow that has periodic variation in its velocity profile. The most popular type of these flows is cardiovascular flows. This type of flow can also be found in other systems, such as car engines. Womersley first studied this flow in his work about blood flow in the cardiovascular system.

Pulsatile flow has been proven to stimulate the bone cells by its induced wall shear stress. However, this interaction was left relatively unnoticed by scientists at the time. It is essential to obtain kinetic properties of the pulsatile flow over the bone cell to have a better understanding of the possible method of the response of the bone cell to the wall shear stress and velocity field. In this dissertation, we will investigate one particular case of pulsatile flow over the bone cell. The physical properties of the problem are taken from the Biomedical Engineering Department of Purdue School of Engineering and Technology. In the first step, we will validate our model and use it to simulate the blood flow over the cell. Oscillatory flow is a subcategory of pulsatile flow. In this study, we are going to use the oscillatory blood flow for simplicity to simulate the blood flow over the cell. .

3.2.2 Analytical solution and computational validation

In this dissertation, we are going to simulate the oscillatory blood flow over the bone cell. We will use geometry with the dimensions of the physical problem and use the lattice Boltzmann method in the simulation of wall shear stress and velocity field around the cell. This lattice Boltzmann code was developed by the research team of Professor Whitney Yu at the mechanical and energy engineering department at Indiana University-Purdue University Indianapolis. This code computationally solves the lattice Boltzmann equations in the GPU, and most programming has been done on GPU In this section, we need to use the analytical solution as an accurate and

reliable answer to check our code's validity. As was mentioned before, the considered geometry for the blood flow in a rectangular duct. Several studies have investigated the analytical solution of oscillatory flow in a rectangular cross-section: The Navier-Stokes equation for rectangular duct is:

$$\rho\frac{\partial w}{\partial t} - \mu(\frac{\partial^2 w}{\partial y^2} + \frac{\partial^2 w}{\partial x^2}) = \frac{\partial p}{\partial z}(t) \tag{3.52}$$

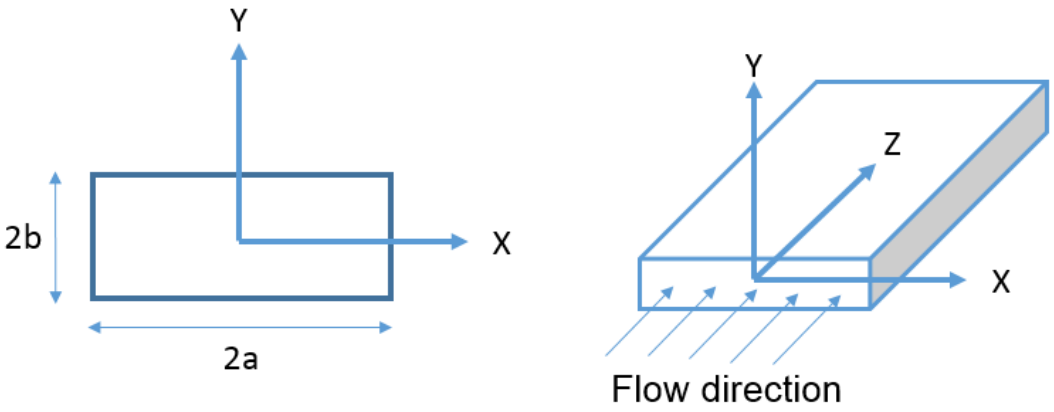

Fig. 3.3. The rectangular duct and attached coordination on it

In which ρ is the density of the flow, w is the velocity of the fluid in the Z direction, μ is the viscosity of the fluid, x and y are the locations in X and Y directions, respectively and $\frac{\partial p}{\partial z}(t)$ is the pulsatile pressure gradient in the duct which is the function of time (t). Since the flow is the simple oscillatory flow, the pressure gradient can be written as:

$$\frac{\partial p}{\partial z}(t) = \frac{dp}{dz} sin(\omega t + \phi) \tag{3.53}$$

In which $\frac{dp}{dz}$ is the pressure gradient amplitude (constant), ω is the angular oscillation speed of flow, and ϕ is the phase of the flow and can be determined from the boundary condition of the fluid. The equation (1) can be non-dimensionalized as the following equation:

$$\beta^2\frac{\partial \bar{w}}{\partial \bar{t}} = e^{i\bar{t}} + (\frac{\partial^2 \bar{w}}{\partial \bar{x}^2} + \frac{\partial^2 \bar{w}}{\partial \bar{y}^2}) \tag{3.54}$$

$$\beta = b(\omega/\nu)^{0.5} \tag{3.55}$$

$$\bar{x} = \frac{x}{b} \tag{3.56}$$

$$\bar{y} = \frac{y}{b} \tag{3.57}$$

$$\bar{t} = t\omega \tag{3.58}$$

$$\lambda = \frac{a}{b} \tag{3.59}$$

$$\bar{w} = \frac{w}{Pb^2}\nu \tag{3.60}$$

$$\beta = b(\omega/\nu)^{0.5} \tag{3.61}$$

In which β is called the reduced frequency, $\bar{w}$ is the non-dimensional velocity, $\bar{t}$ is the non-dimensional time, Re is the Reynolds number, $\bar{x}$ is the non-dimensional distance in X direction and $\bar{y}$ is non-dimensional distance in Y direction the solution is assumed to have one steady and periodic component:

$$\bar{w}(\bar{x}, \bar{y}, \bar{t}) = \bar{W}(\bar{x}, \bar{y})e^{i\bar{t}} \tag{3.62}$$

With this assumption, the analytical solution for this problem will be:

$$\begin{aligned} \bar{W}(\bar{x}, \bar{y}) = \frac{4}{\pi}\sum_{n=0}^{\infty}\frac{(-1)^n}{(2n+1)p^2}(1 + \frac{1}{\sin(D\cdot\lambda)} \\ [e^{\frac{D}{2}\bar{x}}\sinh(-\frac{D}{2}\lambda) - e^{-\frac{D}{2}\bar{x}}\sinh(\frac{D}{2}\lambda)])\cos(\frac{2n+1}{2}\pi\bar{y}) \end{aligned} \tag{3.63}$$

$$p^2 = i\beta^2 + (\frac{2n+1}{2}\pi)^2 \tag{3.64}$$

$$D = 2p \tag{3.65}$$

Now we have the velocity distribution in the rectangular duct, so it is easy to calculate the wall shear stress inside the duct. By taking the derivative with respect to the y from the velocity equation, we would have:

$$\begin{aligned} \tau = \frac{4b^2}{\pi}\frac{dp}{dz}\sum_{n=1}^{\infty}\frac{(-1)^n}{(2n+1)p^2}[1 + \frac{1}{sinh(D\cdot\lambda)}[e^{\frac{D}{2}\bar{x}}sinh(-\frac{D\lambda}{2}) - e^{\frac{-D}{2}\bar{x}}sinh(\frac{D\lambda}{2})]] \\ \times -sin(\frac{2n+1}{2}\pi\bar{y})\frac{2n+1}{2}\frac{\pi}{b} \end{aligned} \tag{3.66}$$

Which is the wall shear stress over the wall in a rectangular channel. Using the Navier-Stokes equation, we can obtain the velocity profile equation for the oscillating flow between two parallel plates as [45]:

$$u(y,t) = -\frac{1}{\rho}\frac{dp}{dz}\frac{e^{i\omega t}}{i\omega}[1 - \frac{cosh(y\sqrt{i\omega/\nu})}{cosh(b\sqrt{i\omega/\nu})}] \tag{3.67}$$

by taking the derivative with respect to y, we can obtain the wall shear stress on the wall over time:

$$\tau = \nu\frac{dp}{dz}\frac{e^{i\omega t}}{i\omega}[\frac{sinh(y\sqrt{i\omega/\nu})}{cosh(b\sqrt{i\omega/\nu})}]\sqrt{i\omega/\nu} \tag{3.68}$$

3.2.3 Mechanical properties of the problem

This data is provided by the Department of Biomedical Engineering research team. To start the simulation, we need to know all the geometrical and physical parameters. The assumed for the flow is a rectangular duct. Since the flow is fully developed in most of its way through the duct, we only focus on the solution of the problem in the $X - Y$ plane. The geometry sizes are given in Fig. 3.5., and the physical parameters are given in Table 3.1.

3.2.4 The transformation of volume the flow rate to the pressure gradient

We obtained the analytical solution in section 3.2.2, but to use the data given in section 3.6.2. we need to extract the maximum pressure gradient from the average flow rate. The pure oscillatory nature of the flow is essential in our calculation. The relationship between the maximum pressure gradient and the average flow rate is:

$$\frac{dP}{dz} = \frac{1}{T}\int \frac{dp}{dz}\sin(\omega t)dt = 2\int \frac{dp}{dz}\sin(2\pi t)dt = 7886Pa/s \tag{3.69}$$

$$\frac{dP}{dz} = \frac{12\mu Q}{bh^3} = 5021.3Pa/s \tag{3.70}$$

$$\frac{dp}{dz} = 7887Pa/s \tag{3.71}$$

Table 3.1.
Physical property of the system

The maximum speed of the flow	0.1228 m/s
density of the blood	1000 kg/m^3
blood kinematic viscosity	$0.72 \times 10^{-}6m^2/s$
volume flow rate	$0.59 \times 10^{-}6m^3/s$
angular oscillation speed of flow (ω)	2π
width of the duct (2a)	$37.6mm$
volume flow rate	$0.59 \times 10^{-}6m^3/s$
height of the duct (2b)	$0.3mm$

In which $\frac{dP}{dz}$ is the amplitude of the pressure.

3.2.5 Transforming the STL file to P-value data

To import geometry in our code, we need to transform the geometry into a matrix of P-values. The amount of P-value for the solid part of the geometry equals one, and the fluid portion of the geometry equals zero. The P-value is between Zero and One for the boundary cell in which the wall can pass the cell at any angle and direction. The Solidworks software has been used in this dissertation to model. The produced geometry will later be transformed into P-value data. This is done by the STL2Pvalue code, which has been developed in the research team of Dr. Whitney Yu at the mechanical and energy engineering of Indiana University-Purdue University, Indianapolis. This code takes the STL format of the designed CAD and transforms it into a P-value matrix that can be used as an input in our code. This code reads the CAD, and based on the desired resolution that we order, it produces a mesh, and for every single cell of that mesh, we get the following information about the geometry:

- Column one: the P-value

- Column two: if the cell is a boundary cell the normal vector of the surface in the cell in the X direction.
- Column three: if the cell is a boundary cell the normal vector of the surface in the cell in the Y direction.
- Column four: if the cell is a boundary cell the normal vector of the surface in the cell in the Z direction.
- Column five: if the cell is a boundary cell it gives the distance of the center of the cell from the surface.

The output file of the STL2Pvalue code also contains information about the mesh resolution in each direction. To verify the accuracy of the transformed geometry to P-value data, use the volume comparison. The volume of the geometry is known, and the dimensions were given in the CAD software. The goal is to compare this volume with the volume calculated from the P-value data. To make the comparison, we have started designing a cubic geometry with a sphere centered inside it.

If we sum the amount of P-value for all the cells in the entire domain, we will obtain the solid volume of the space, which in this problem is the volume of the sphere. Considering that each cell that is entirely inside the sphere has the P-value equal to one, the summation of P-values inside the sphere gives the number of the cells inside the sphere. By having the total number of the cells in the domain and dividing the number of the cells inside the sphere to the total number of the cells, we can get the volumetric ratio of the sphere to the cube. This volumetric ratio can be easily be obtained from the dimensions given to the geometry and be compared to the P-value results.

$$\frac{\Sigma Pvalue}{Number\ of\ the\ cells} = \frac{\Sigma_{fluid} Pvalue + \Sigma_{solid} Pvalue}{Number\ of\ the\ cells} \tag{3.72}$$

The summation of P-values for the fluid part is zero, therefore we can simplify equation (3.70) as:

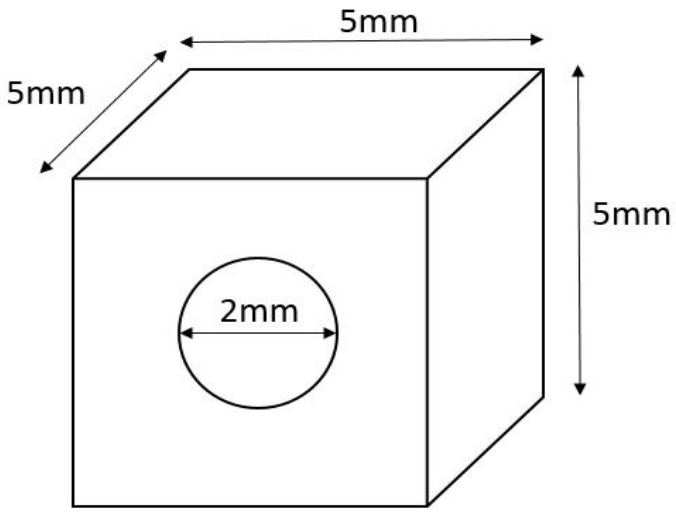

Fig. 3.4. The rectangular cube and the internal sphere inside it. We have chosen P-value equal to one for the spherical structure inside the sphere, and P-value equals zero for the rest of the domain out of the sphere and inside the cube.

$$= \frac{\Sigma_{solid} Pvalue}{Number\ of\ the\ cells} = \frac{volume\ of\ the\ solid\ sphere}{volume\ of\ the\ cube} \tag{3.73}$$

The Table 3.2. shows the accuracy of is this code against the number of cells.

Table 3.2.
Mesh resolution check

Mesh resolution	percentage of error(%)
24*24*24	2.1
32*32*32	0.77
49*49*49	0.45
70*70*70	0.41
82*82*82	0.45
99*99*99	0.40

The next step after confirming the accuracy of the imported geometry is validating the LBM code. The validation has been done for the centerline velocity, and the wall shear stress at the lower wall's center. Keep in mind that this is not the optimum mesh to get the best result for the computational calculation, but it tells you that what number of mesh we need to represent the designed geometry with the least amount of error.

3.2.6 Geometry and boundary condition

The dimensions of the problem are taken from the biomedical engineering department of Indiana University-Purdue University Indianapolis. The dimensions and flow direction are shown in the following figure.

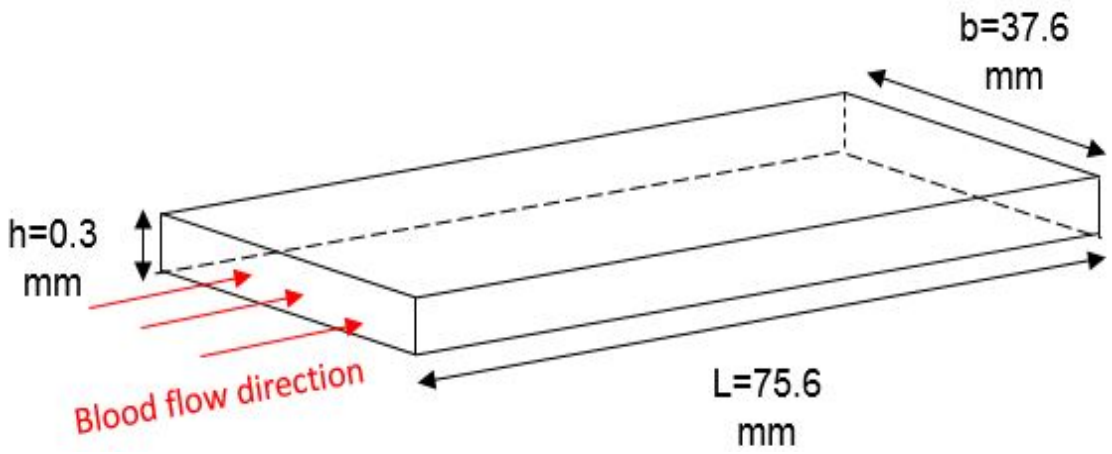

Fig. 3.5. The rectangular duct used for the validation of the LBM code.

As you can see from the dimensions, the width of the geometry (b) is about 1000 times larger than the height of the geometry (h). The Length of the geometry (L) is also around 2000 times larger than the height (h). If we use any coarse or fine mesh to cover the side (h), we use many cells. Thus we need to use a smaller geometry that represents the mechanical properties of the main problem. If we choose one percent as the limit in error in center-line velocity and the wall shear stress, we will have the

cross-section, as shown in Fig. 3.6. Moreover, the pressure gradient has also been obtained from section 3.6.3. The actual problem contains the information about the volume flow rate, but because the used parameter in the computational code is the pressure gradient, we focus on the pressure gradient behavior, and its graph is as shown in Fig. 3.7.

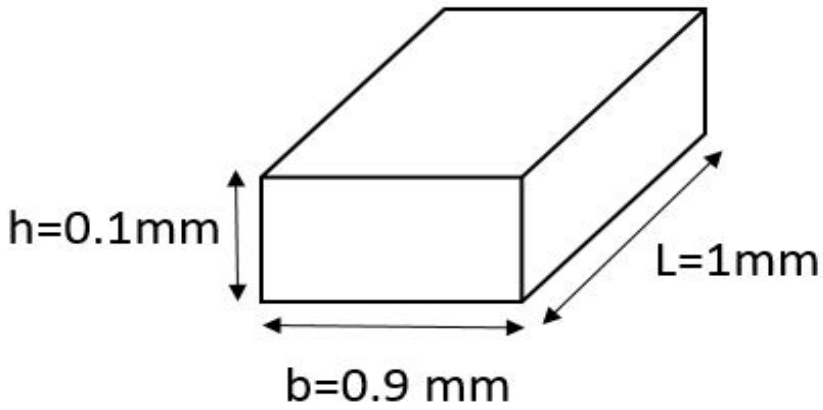

Fig. 3.6. The rectangular duct used for the validation of the LBM code.

3.2.7 Mesh and time step check

The next part of making sure about the validity of our code is the mesh resolution. The optimal mesh size has been chosen regarding Table 3.3. of the results. This tells

Table 3.3.
Mesh resolution check for computation

Mesh resolution (h*b*L)	percentage of error(%)
10*30*30	1.6
20*60*60	0.6
30*90*90	<0.1

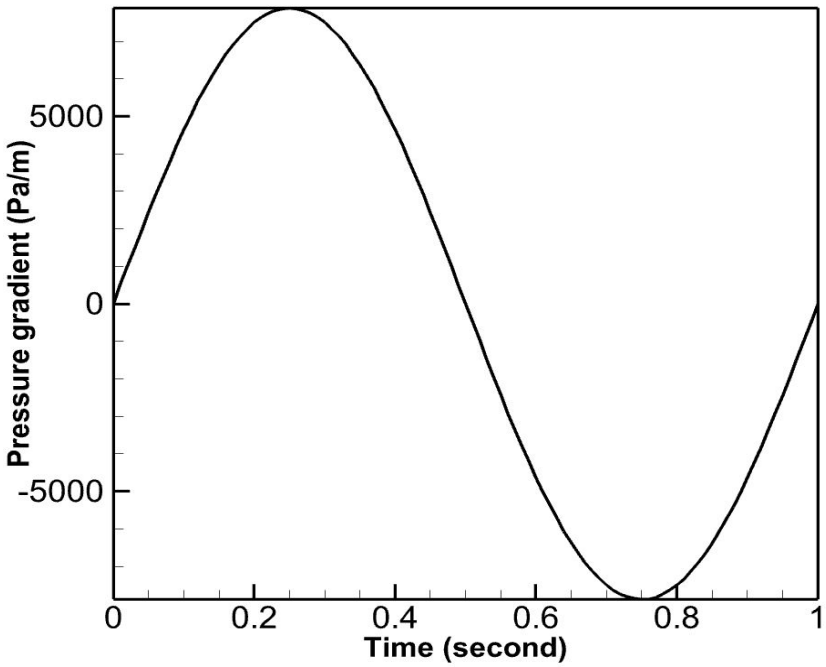

Fig. 3.7. The pressure gradient variation inside the rectangular duct.

us the appropriate number of mesh cells for our geometry is 30*90*90.

Table 3.4.
Time step resolution check

Time step (second)	percentage of error(%)
1/500	1.7
1/1000	0.4
1/1500	<0.1

3.2.8 Wall shear stress calculation

Although the case of the validation is a simple duct with parallel walls and we can simply discrete the equations over it, this is not always the case. There are

many circumstances in which we encounter a geometry with a complex surface. The problem with these surfaces is that the computational cells are not necessarily aligned with the normal vector of the surface and so we cannot simply compute the wall shear stress along the normal vector. Instead of using the velocity field and discrediting it, we will calculate the strain rate and wall shear stress directly from the lattice Boltzmann equation. The strain rate equation, according to LBM formula, will be:

$$\begin{aligned} S_{\alpha\beta} &= -\frac{1}{2\rho\tau c_s^2}\sum_i e_{i\alpha}e_{i\beta}(f_i - f_i^{eq}) \\ &= -\frac{3}{2N\tau}\Sigma_i e_{i\alpha}e_{i\beta}(n_i - n_i^{eq}) \end{aligned} \tag{3.74}$$

In which N is the number of particles in the cell, $e_{i\alpha}$ and $e_{i\beta}$ represent the particle streaming directions. The shear stress is:

$$\sigma_{\alpha\beta} = 2\mu S_{\alpha\beta}$$

The viscosity equation in lattice Boltzmann can also be calculated like:

$$\mu = \nu\rho = \frac{1}{3}(\tau - \frac{1}{2}) \tag{3.76}$$

In which ρ is the lattice density and equals to one. Total stress can be calculated from the following equation:

$$T_{\alpha\beta} = -p\delta_{\alpha\beta} + \sigma_{\alpha\beta} \tag{3.77}$$

In which $\delta_{\alpha\beta}$ is the Kronecker delta function.

The wall shear stress relation will be:

$$WSS_\alpha = T_{\alpha\beta}n_\beta - (n_\beta T_{\gamma\beta}n_\gamma)n_\alpha \tag{3.78}$$

3.2.9 Velocity and wall shear stress validation

Now that we have obtained the optimum resolution for the mesh number and the time step, we compare the analytical solution with the LBM code's computational results. The analytical solutions have been obtained in section 3.3.2, and we use equations 3.63 and 3.66 to validate the computational results. Fig. 3.8. shows the validation of the computational code versus the results of analytical solution (equation 3.63), for the center-line velocity. The computational code for the wall shear stress has been validated in Fig. 3.9. against the analytical solution. Finding a model that catches the wall shear stress accurately can be a challenging task. In this section, we compare the results that we get from the LBM and challenge its power by comparing its results with the results of the finite difference method (FDM). Other computational models, such as the finite volume method or finite element method (FEM), can also be used in further research to find the best computational model in studying wall shear stress. We have studied the wall shear stress in the three boundary cells beside the wall. This is done because the velocity and the moment at the first boundary cell are very small, and thus it can introduce larger errors in computing the wall shear stress. We study the first to third cell to see how the distance from the boundary cell is effective in reducing the computational error. By looking at Table 3.5. we can realize the interesting behavior in the second boundary cell where we observe the least computational error in the wall shear stress value. This can only be seen in the LBM and the error grows in FDM by moving normal to the boundary cell. In Fig. 3.10. you can see the comparison between the results of the computational code and the analytical solution. The analytical solution for the WSS in parallel plates is also added to study the effect of the corners. We have used the results of equation 3.68 in order to plot the wall shear stress between parallel plates. In geometries where the width (a) is much higher than the height (b), we must see the same behavior in velocity and consequently, the wall shear stress as we see in the flow between parallel plates.

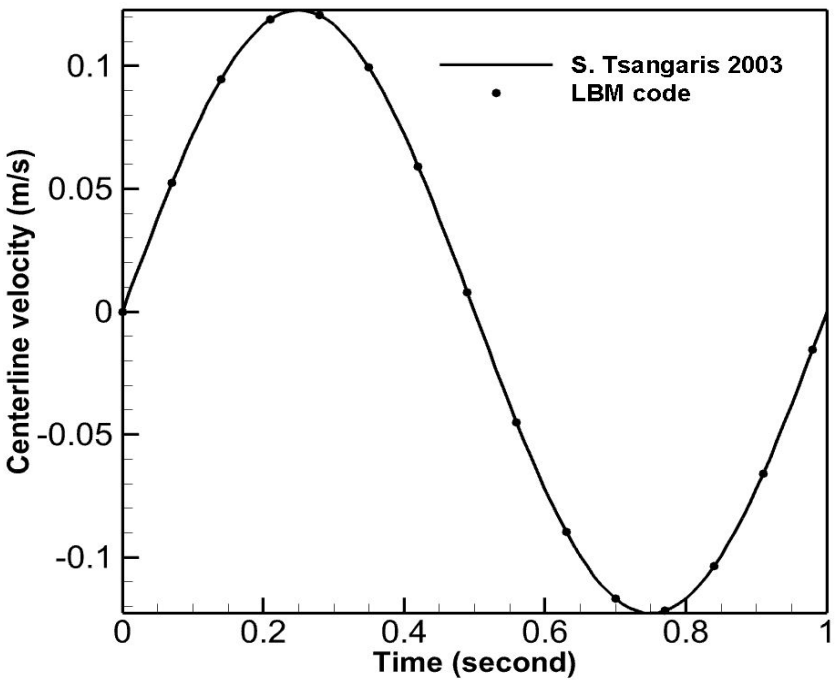

Fig. 3.8. The comparison between the velocities at the center-line using analytical solution (equation (3.63)), and the computational code, Error=0.1 %

Table 3.5.
wall shear stress accuracy study

	Velocity error(%)	LBM WSS error(%)	FDM WSS error (%)
1^{st} *boundary cell*	0.1 %	0.1%	2.7 %
2^{nd} *boundary cell*	0.1 %	0.06 %	2.9 %
3^{nd} *boundary cell*	0.1 %	0.25 %	3.1 %

3.3 Conclusion

The wall shear stress is a parameter that depends on the gradient of the velocity beside the wall thus to obtain an accurate wall shear stress, we need to have an accurate model that predicts the velocity very well. The Importance of this work is

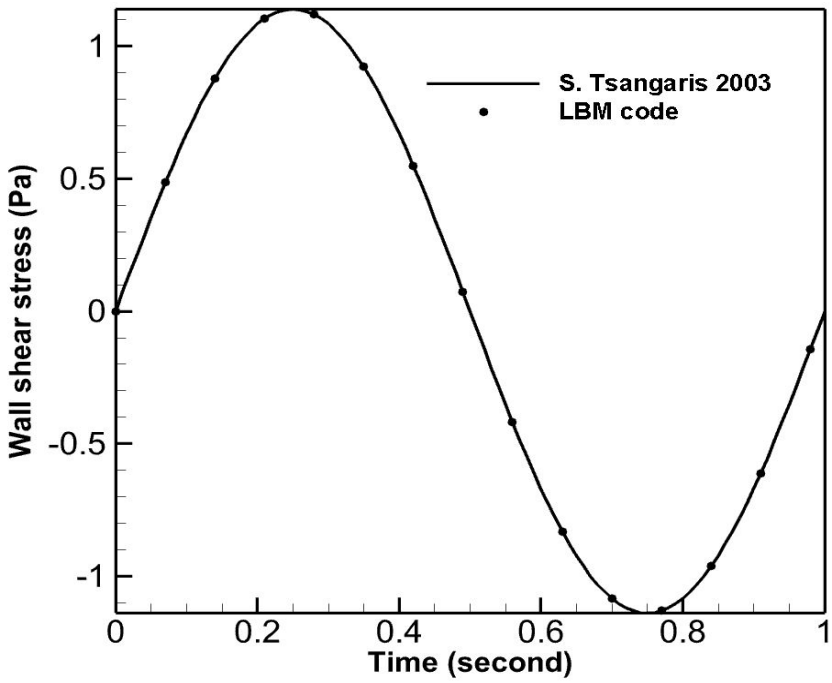

Fig. 3.9. The comparison between the wall shear stress at the lower (Or upper) wall using analytical solution (equation (3.66)), and the computational cod, Error=0.1 %

that we have calculated the wall shear stress and investigated it in detail. Although the results in the first cell have small error (less than one percent), the error in the second cell is even smaller. These shear stress results has came directly from the lattice Boltzmann method and were compared to the results of finite difference method. The results show that the lattice Boltzmann method is highly more accurate than the results in the finite difference method. In all three boundary cells that we have studied, the error of the model coming from LBM is smaller compared to the results coming from the FDM. We have also indicated that the wall shear stress result of parallel plates and rectangular channel have relatively the same value at the mid-section of the wall. It can be predicted that for larger geometries, the wall shear stress at mid-section of the geometry stays close to the wall shear stress in parallel plates. However, this immediately changes while we move along the X axis and get far from the midsection of the wall due to the effects of the side walls. The wall shear stress

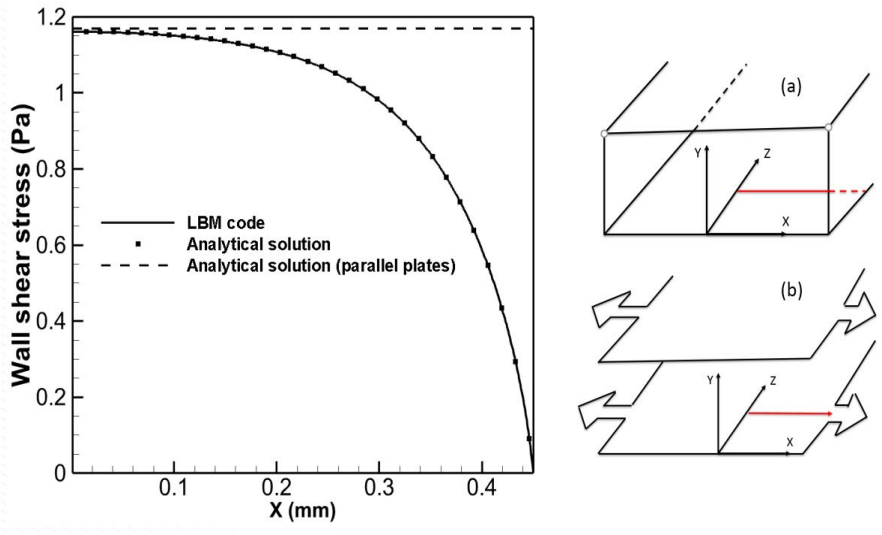

Fig. 3.10. The validation results for the wall shear stress along the X axis. The LBM simulation is done for case (a) and the results of WSS are measured along the red line in the X axis and compared to the analytical solution shown with the square symbol.

drops to zero close to the corners. This result makes sense on account of the fact that close to the corner the velocity is zero in X and Y direction (non-slip boundary condition close to the wall) and consequently there is no gradient of velocity in any direction along $X - Y$ plane.

4. SUMMARY

This work studied the computational fluid dynamics and its application in two different bio-engineering cases. At the beginning we dealt with finding an optimum model to study the drug diffusion in the posterior eye to treat Age-related macular degeneration which is chronic disease and is more common in elders. We have covered the possible treatment methods and determined that using drug implant storage at the posterior eye is one the methods with least side effects. The current most common treatment method right now is the direct injection of the drug to the eye which can have serious side effects such as retinal detachment or internal eye bleeding. By using CFD, we can get valuable information about the drug behavior during the treatment and this may replace the common injection method with widely utilized drug implants. After obtaining a good computational model, we use this model to study the drug delivery after adding a porous divider to the system. We use this porous divider as a modifier in controlling the drug delivery. This modifier contains several pores and the pore size and diffusion coefficient are the governing parameters in controlling the drug delivery. By using the validated computational model we could see the effects of adding pores to the drug implant. The following questions will remain to answer: what is the optimum geometry to have a more uniform drug delivery? what are the effects of drug molecular weight? what is the effect of the pore thickness? these questions need further research to be answered. We have used the lattice Boltzmann method to obtain the wall shear stress and velocity in the next part. The second part tackles with the creation and import of a geometry and building P-value out of CAD file. The validity of this transforming code has been verified in the second part. We have obtained a highly accurate model in the lattice Boltzmann to capture the wall shear stress. We later obtained that the wall shear stress in validation is more accurate at the second cell right beside the boundary cell. This can be attributed to

the fact that the velocity at the boundary cell is very small and due to the fact that wall shear stress is about the velocity gradient at the wall, it is harder to have an accurate computational model at the boundary.

REFERENCES

[1] A. Urtti, "Challenges and obstacles of ocular pharmacokinetics and drug delivery," *Advanced drug delivery reviews*, vol. 58, no. 11, pp. 1131–1135, 2006.

[2] T. Vaughan, M. Haugh, and L. McNamara, "A fluid–structure interaction model to characterize bone cell stimulation in parallel-plate flow chamber systems," *Journal of The Royal Society Interface*, vol. 10, no. 81, p. 20120900, 2013.

[3] D. H. Geroski and H. F. Edelhauser, "Drug delivery for posterior segment eye disease," *Investigative ophthalmology & visual science*, vol. 41, no. 5, pp. 961–964, 2000.

[4] I. Ahmed and T. Patton, "Importance of the noncorneal absorption route in topical ophthalmic drug delivery." *Investigative ophthalmology & visual science*, vol. 26, no. 4, pp. 584–587, 1985.

[5] M. E. Myles, D. M. Neumann, and J. M. Hill, "Recent progress in ocular drug delivery for posterior segment disease: emphasis on transscleral iontophoresis," *Advanced drug delivery reviews*, vol. 57, no. 14, pp. 2063–2079, 2005.

[6] A. Patel, K. Cholkar, V. Agrahari, and A. K. Mitra, "Ocular drug delivery systems: an overview," *World journal of pharmacology*, vol. 2, no. 2, p. 47, 2013.

[7] J. Ambati, E. S. Gragoudas, J. W. Miller, T. T. You, K. Miyamoto, F. C. Delori, and A. P. Adamis, "Transscleral delivery of bioactive protein to the choroid and retina," *Investigative ophthalmology & visual science*, vol. 41, no. 5, pp. 1186–1191, 2000.

[8] J. M. Conrad and J. R. Robinson, "Aqueous chamber drug distribution volume measurement in rabbits," *Journal of pharmaceutical sciences*, vol. 66, no. 2, pp. 219–224, 1977.

[9] J. Miller, W. Wilson, C. Wilson, and D. Uttamchandani, "Minimally invasive, direct, real time measurement of drug concentration in the anterior eye," *British journal of ophthalmology*, vol. 89, no. 9, pp. 1147–1151, 2005.

[10] C. B. Engler, B. Sander, M. Larsen, P. Dalgaard, and H. Lund-Andersen, "Fluorescein transport across the human blood-retina barrier in the direction vitreous to blood: Quantitative assessment in vivo," *Acta ophthalmologica*, vol. 72, no. 6, pp. 655–662, 1994.

[11] M. E. Kavousanakis, N. G. Kalogeropoulos, and D. T. Hatziavramidis, "Computational modeling of drug delivery to the posterior eye," *Chemical Engineering Science*, vol. 108, pp. 203–212, 2014.

[12] R. K. Balachandran and V. H. Barocas, "Computer modeling of drug delivery to the posterior eye: effect of active transport and loss to choroidal blood flow," *Pharmaceutical research*, vol. 25, no. 11, pp. 2685–2696, 2008.

[13] J. Kathawate and S. Acharya, "Computational modeling of intravitreal drug delivery in the vitreous chamber with different vitreous substitutes," *International Journal of Heat and Mass Transfer*, vol. 51, no. 23-24, pp. 5598–5609, 2008.

[14] E. Jooybar, M. J. Abdekhodaie, F. Farhadi, and Y.-L. Cheng, "Computational modeling of drug distribution in the posterior segment of the eye: effects of device variables and positions," *Mathematical biosciences*, vol. 255, pp. 11–20, 2014.

[15] P. J. Missel, "Simulating intravitreal injections in anatomically accurate models for rabbit, monkey, and human eyes," *Pharmaceutical research*, vol. 29, no. 12, pp. 3251–3272, 2012.

[16] P. R. Ninawe, D. Hatziavramidis, and S. J. Parulekar, "Delivery of drug macromolecules from thermally responsive gel implants to the posterior eye," *Chemical Engineering Science*, vol. 65, no. 18, pp. 5170–5177, 2010.

[17] H. Kourlas and P. Abrams, "Ranibizumab for the treatment of neovascular age-related macular degeneration: a review," *Clinical therapeutics*, vol. 29, no. 9, pp. 1850–1861, 2007.

[18] I. Fatt and B. O. Hedbys, "Flow of water in the sclera," *Experimental eye research*, vol. 10, no. 2, pp. 243–249, 1970.

[19] S. Tsuboi, "Measurement of the volume flow and hydraulic conductivity across the isolated dog retinal pigment epithelium." *Investigative ophthalmology & visual science*, vol. 28, no. 11, pp. 1776–1782, 1987.

[20] X. He and L.-S. Luo, "Theory of the lattice boltzmann method: From the boltzmann equation to the lattice boltzmann equation," *Physical Review E*, vol. 56, no. 6, p. 6811, 1997.

[21] Z. Guo and C. Shu, *Lattice Boltzmann method and its applications in engineering*. World Scientific, 2013, vol. 3.

[22] Y.-H. Qian, D. d'Humières, and P. Lallemand, "Lattice bgk models for navier-stokes equation," *EPL (Europhysics Letters)*, vol. 17, no. 6, p. 479, 1992.

[23] U. Frisch, B. Hasslacher, and Y. Pomeau, "Lattice-gas automata for the navier-stokes equation," *Physical review letters*, vol. 56, no. 14, p. 1505, 1986.

[24] L. Li-Shi, "The lattice-gas and lattice boltzmann methods: past, present, and future," *ICASE, Mail Stop C*, vol. 132, 2000.

[25] G. R. McNamara and G. Zanetti, "Use of the boltzmann equation to simulate lattice-gas automata," *Physical review letters*, vol. 61, no. 20, p. 2332, 1988.

[26] F. J. Higuera and J. Jiménez, "Boltzmann approach to lattice gas simulations," *EPL (Europhysics Letters)*, vol. 9, no. 7, p. 663, 1989.

[27] H. Chen, S. Chen, and W. H. Matthaeus, "Recovery of the navier-stokes equations using a lattice-gas boltzmann method," *Physical review A*, vol. 45, no. 8, p. R5339, 1992.

[28] B. Keating, G. Vahala, J. Yepez, M. Soe, and L. Vahala, "Entropic lattice boltzmann representations required to recover navier-stokes flows," *Physical Review E*, vol. 75, no. 3, p. 036712, 2007.

[29] Z. Guo, B. Shi, and N. Wang, "Lattice bgk model for incompressible navier–stokes equation," *Journal of Computational Physics*, vol. 165, no. 1, pp. 288–306, 2000.

[30] Q. Li, Y. He, Y. Wang, and W. Tao, "Coupled double-distribution-function lattice boltzmann method for the compressible navier-stokes equations," *Physical Review E*, vol. 76, no. 5, p. 056705, 2007.

[31] S. Zhan, Y. Su, Z. Jin, M. Zhang, W. Wang, Y. Hao, and L. Li, "Study of liquid-liquid two-phase flow in hydrophilic nanochannels by molecular simulations and theoretical modeling," *Chemical Engineering Journal*, p. 125053, 2020.

[32] Y. Zheng, A. L. Garcia, and B. J. Alder, "Comparison of kinetic theory and hydrodynamics for poiseuille flow," *Journal of Statistical Physics*, vol. 109, no. 3-4, pp. 495–505, 2002.

[33] S. Harris, *An introduction to the theory of the Boltzmann equation*. Courier Corporation, 2004.

[34] P. Lallemand and L.-S. Luo, "Theory of the lattice boltzmann method: Dispersion, dissipation, isotropy, galilean invariance, and stability," *Physical Review E*, vol. 61, no. 6, p. 6546, 2000.

[35] H. Yu, "Lattice boltzmann equation simulations of turbulence, mixing, and combustion," Ph.D. dissertation, Texas A&M University, 2006.

[36] E. Lauga and T. R. Powers, "The hydrodynamics of swimming microorganisms," *Reports on Progress in Physics*, vol. 72, no. 9, p. 096601, 2009.

[37] S. Chen and G. D. Doolen, "Lattice boltzmann method for fluid flows," *Annual review of fluid mechanics*, vol. 30, no. 1, pp. 329–364, 1998.

[38] A. J. Ladd, "Numerical simulations of particulate suspensions via a discretized boltzmann equation. part 1. theoretical foundation," *Journal of fluid mechanics*, vol. 271, pp. 285–309, 1994.

[39] C. K. Aidun and Y. Lu, "Lattice boltzmann simulation of solid particles suspended in fluid," *Journal of statistical physics*, vol. 81, no. 1-2, pp. 49–61, 1995.

[40] C. K. Aidun and J. R. Clausen, "Lattice-boltzmann method for complex flows," *Annual review of fluid mechanics*, vol. 42, pp. 439–472, 2010.

[41] B. Crouse, D. M. Freed, N. Koliha, G. Balasubramanian, R. Satti, D. Bale, and S. Zuklic, "A lattice-boltzmann based method applied to digital rock characterization of perforation tunnel damage," in *Paper SCA2016-058 presented at the International Symposium of the Society of Core Analysts held in Snow Mass, Colorado, USA*, 2016.

[42] Y. Li, R. Shock, R. Zhang, and H. Chen, "Numerical study of flow past an impulsively started cylinder by the lattice-boltzmann method," *Journal of Fluid Mechanics*, vol. 519, p. 273, 2004.

[43] Y. Li, R. Zhang, R. Shock, and H. Chen, "Prediction of vortex shedding from a circular cylinder using a volumetric lattice-boltzmann boundary approach," *The European Physical Journal Special Topics*, vol. 171, no. 1, pp. 91–97, 2009.

[44] H. Yu, X. Chen, Z. Wang, D. Deep, E. Lima, Y. Zhao, and S. D. Teague, "Mass-conserved volumetric lattice boltzmann method for complex flows with willfully moving boundaries," *Physical Review E*, vol. 89, no. 6, p. 063304, 2014.

[45] J. Majdalani, "Exact navier-stokes solution for the pulsatory viscous channel flow with arbitrary pressure gradient," *Journal of propulsion and power*, vol. 24, no. 6, pp. 1412–1423, 2008.

PUBLICATION

PUBLICATION

- Abootorabi, Tripathi, Yu, and Davila, Computational Modeling of Intraocular Drug Delivery Supplied by Porous Implants, Drug Delivery and Translational Research, submitted, 2020
- (Poster) S. Abootorabi, A. Tripathi, L. Davila, and H. Yu, "Effects of implant separator structure on drug delivery
- (Oral presentation) X. Zhang, S. A. Abootorabi, H. Yokota, and H. Yu, Preliminary Study for Wall-shear Stress of Pulsatile Flows in 3-D Ducts, The 72nd Annual Meeting of the American Physical Society's Division of Fluid Dynamics,

ACKNOWLEDGEMENT

ACKNOWLEDGEMENT

This project has been supported by the following resources:

- National Science Foundation under grant No. 1803845.
- IU-STEM via faculty collaborative award
- The Extreme Science and Engineering Discovery Environment (XSEDE) which is supported by National Science Foundation Grant No. ACI-1548562

VITA

VITA

Arya Abootorabi received Bachelor of Science in Mechanical Engineering from Amirkabir University of technology. During his bachelor degree, he received silver nationwide Olympiad medal in physics in 2012 and was the founder and director of Amirkabir university of technology journal club from 2017 to 2018. He then joined University of Tehran-IUPUI joint program for the Master's degree and finished his first year at university of Tehran with perfect GPA. He then joined IUPUI for the rest of his Master's degree and became a research assistant at CFD lab (Head Prof. Huidan Yu). He has published three papers in his 1.5 year period of research at IUPUI and has got grade A in all the courses he passed at IUPUI.